

# JGR Atmospheres

## RESEARCH ARTICLE

10.1029/2019JD030287

### Key Points:

- Turbulence parameters are estimated in the free atmosphere using Thorpe analysis and high vertical-resolution radiosonde data in the United States
- Characteristics of vertical, statistical, and horizontal distributions and long-term variability of turbulence parameters are examined

### Supporting Information:

- Supporting Information S1

### Correspondence to:

H.-Y. Chun,  
chunhy@yonsei.ac.kr

### Citation:

Ko, H.-C., Chun, H.-Y., Wilson, R., & Geller, M. A. (2019). Characteristics of atmospheric turbulence retrieved from high vertical-resolution radiosonde data in the United States. *Journal of Geophysical Research: Atmospheres*, 124, 7553–7579. <https://doi.org/10.1029/2019JD030287>

Received 11 JAN 2019

Accepted 12 JUN 2019

Accepted article online 5 JUL 2019

Published online 24 JUL 2019

### Author Contributions:

**Conceptualization:** H.-C. Ko, H.-Y. Chun





**Formal analysis:** H.-C. Ko, H.-Y. Chun, R. Wilson

**Investigation:** H.-C. Ko, H.-Y. Chun, R. Wilson

**Writing - original draft:** H.-C. Ko, H.-Y. Chun

**Writing - review & editing:** H.-C. Ko, H.-Y. Chun, R. Wilson, M. A. Geller

## Characteristics of Atmospheric Turbulence Retrieved From High Vertical-Resolution Radiosonde Data in the United States

H.-C. Ko<sup>1</sup> , H.-Y. Chun<sup>1</sup> , R. Wilson<sup>2</sup> , and M. A. Geller<sup>3</sup> 

<sup>1</sup>Department of Atmospheric Sciences, Yonsei University, Seoul, South Korea, <sup>2</sup>LATMOS/IPSL, Sorbonne Université, CNRS, Paris, France, <sup>3</sup>School of Marine and Atmospheric Sciences, Stony Brook University (retired), Stony Brook, NY, USA

**Abstract** In this study, we estimate atmospheric turbulence in the free atmosphere in terms of the Thorpe scale ( $L_T$ ) and eddy dissipation rate ( $\epsilon$ ) using U.S. high vertical-resolution radiosonde data over 4 years (September 2012 to August 2016) at 68 operational stations. In addition, same calculations are conducted for 12 years (October 2005 to September 2017) at four stations among the 68 stations. These high vertical-resolution radiosonde data have a vertical resolution of approximately 5 m and extend to an altitude of approximately 33 km, and thus, turbulence can be retrieved in the entire troposphere and lower stratosphere. There are thicker and stronger turbulent layers in the troposphere than in the stratosphere, with mean  $\epsilon$  values of  $1.84 \times 10^{-4}$  and  $1.37 \times 10^{-4} \text{ m}^2/\text{s}^3$  in the troposphere and stratosphere, respectively. The vertical structure of  $\epsilon$  exhibits strong seasonal variations, especially in the upper troposphere and lower stratosphere, with the largest  $\epsilon$  values in summer and the smallest in winter. In the horizontal distribution of  $\epsilon$ , large  $\epsilon$  is seen mainly above the mountainous region in the troposphere, but this pattern is not seen in the stratosphere. Although  $\epsilon$  is estimated by the square of  $L_T$  multiplied by the cube of the Brunt-Väisälä frequency ( $N$ ), the regions of large  $\epsilon$  are matched with large  $L_T$  regions where  $N$  is relatively small. For the time series of  $\epsilon$  near the tropopause for 12 years at four stations, an annual variation is prominent at all stations without significant interannual variations. There is, however, a slightly increasing trend of  $\epsilon$  at two stations.

## 1. Introduction

A radiosonde is a balloon-borne instrument that directly observes the basic atmospheric quantities such as pressure, temperature, horizontal wind, and relative humidity (RH). Radiosondes are launched more than twice a day at approximately 800 stations around the world (Durre et al., 2018; Ingleby et al., 2016). Radiosonde data are arguably the most important and essential data source for numerical weather prediction models and have been used in studies of planetary boundary layer height (Seidel et al., 2010; Sorbjan & Balsley, 2008), tropopause structure (Birner, 2006; Birner et al., 2002; Seidel & Randel, 2006; Sunilkumar et al., 2017), and gravity waves (Allen & Vincent, 1995; Chun et al., 2006; Chun et al., 2007; Hamilton & Vincent, 1995; Ki & Chun, 2010; Sato & Yoshiki, 2008; Wang et al., 2005; Wang & Geller, 2003; Yoo et al., 2018). Although high vertical-resolution radiosonde data (HVRRD) have often been required for these studies, due to telecommunication limitations and data storage costs, only data with a lower resolution than actual observational resolution data have been routinely provided to weather prediction agencies (Ingleby et al., 2016). Recently, U.S. operational radiosonde stations have provided HVRRD with 6-s (~30 m vertically) resolution from 1998 to 2011, and since 2005, the United States provided HVRRD with 1-s (~5 m vertically) resolution (Geller et al., 2016; Geller et al., 2017; Geller & Love, 2013). HVRRD can sample much finer atmospheric structures, enabling detailed and novel research that could not have been completed with conventional radiosondes, which only provided standard and significant level data (Geller et al., 2017; Ingleby et al., 2016).

There have been previous efforts to estimate the turbulence in the free atmosphere using HVRRD. The main method that has been previously employed is called Thorpe analysis (after Thorpe, 1977), which was originally used to retrieve the local turbulence in the ocean by comparing the observed density profile and the stably stratified profile created through a vertical re-sorting process. The turbulence parameters that can be calculated from this method are eddy dissipation rate ( $\epsilon$ ) and the Thorpe scale ( $L_T$ ), which is meant

to represent the local overturning scale. Applying Thorpe analysis to the atmosphere, Clayson and Kantha (2008) proposed a method to retrieve the turbulence in the free atmosphere using HVRRD. Typical methods for exploring turbulence have been to use wind and temperature data from instruments attached to aircraft or rockets (Cho et al., 2003; Lilly et al., 1974; Lübken, 1992; Sharman et al., 2014) or from remote sensing using radar or lidar (Bertin et al., 1997; Cohn, 1995; Dehghan et al., 2014; Dehghan & Hocking, 2011; Hocking, 1988; Nastrom & Eaton, 1997; Singh et al., 2008; Smalikho et al., 2005). Direct observations using rockets are scarce, however, because of the high cost and subsequent local concentration in limited areas during occasional dedicated campaign periods (Bertin et al., 1997; Grubišić et al., 2008; Sunilkumar et al., 2015). The number of turbulence observations from commercial aircraft is relatively high, but the data may be biased because aircraft avoid reported or forecasted potential turbulence regions and only provide observations along the main flight routes (Bellenger et al., 2017; Dehghan et al., 2014; Kim & Chun, 2012). On the other hand, turbulence estimation using HVRRD not only enables the use of a large amount of data archived around the world but also enables the use of HVRRD, which will be continuously launched in the future.

Since Clayson and Kantha (2008), several studies have estimated turbulence properties using Thorpe analysis and various HVRRD. Using a slow ascent meter-scale sampling radiosonde from July to August 2008 at the Boulder Atmospheric Observatory (40.0°N, 105.0°W), Balsley et al. (2010) showed that the estimates of the magnitude of turbulence depends on the vertical resolution. In particular, many studies have been conducted in the Indian region. Alappattu and Kunhikrishnan (2010) calculated turbulence in the troposphere using data from radiosondes launched in the Bay of Bengal and the Arabian Sea during the 2006 pre-monsoon season. They found that the upper and lower boundaries of the strong turbulent layers in the upper troposphere correspond well to the tops of the cold-point tropopause and the altitudes at which the lapse rate of potential temperature decreased significantly. Nath et al. (2010) reported the seasonal variation and occurrence rate of turbulence using radiosonde data from April 2006 to March 2009 at the Gadanki station (13.5°N, 79.2°E) on the Indian Peninsula, emphasizing the importance of using 5-m-vertical-resolution data. Using radiosonde data from October 2010 to March 2014 at the Gadanki and Trivandrum (8.5°N, 76.9°E) stations on the Indian Peninsula, Sunilkumar et al. (2015) investigated turbulence characteristics and their seasonal and interannual variations in the troposphere and lower stratosphere. Muhsin et al. (2016) studied diurnal variation of the turbulence with respect to stability in the troposphere and lower stratosphere using the same radiosonde data used in Sunilkumar et al. (2015). They showed that the diurnal variations of turbulence are opposite at these two stations in the lower troposphere; however, the diurnal variations are relatively small in the upper troposphere and lower stratosphere at both stations. Bellenger et al. (2015) retrieved clear-air turbulence (CAT) for dry and wet conditions based on the relatively humidity, using 376 radiosonde profiles that were launched at 3-hr intervals from October to November 2011 in the Indian Ocean (8°S, 80.5°E). CAT in their study refers to turbulence outside moist saturated layers, which are determined by using the method by Zhang et al. (2010), not necessarily in a dry atmosphere. They showed that CAT appeared to be greater under dry conditions than wet conditions and frequently when strong vertical humidity gradients occur. Bellenger et al. (2017) examined the role of gravity waves in turbulence generation using more than 3,500 radiosondes over the Indian Ocean. They showed that gravity waves enable the environmental conditions favorable for turbulence generation by lowering static stability. In addition, a few studies have examined turbulence in China. Liu et al. (2014) analyzed the diurnal variations in turbulence using data from radiosondes launched four times a day for 2 months from May to June 1998 from the Kexue #1 scientific observation ship (6.3°N, 109.8°E) in the South China Sea. They showed a clear correlation between the observed turbulence and the diurnal variation in the mesoscale convective systems and pointed to mesoscale convective systems as a major source of turbulence in the upper troposphere. Using radiosonde data from July to August 2014 at the Bosten Lake (41.89°N, 87.22°E), Sun et al. (2016) reported two radar duct events, which were detected during the radiosonde ascent but disappeared during radiosonde descent. They concluded that turbulent mixing caused by Kelvin-Helmholtz instability (KHI) in the upper part of the low-level jet and by density flow advection are the main causes of each radar duct dissipation event.

Several studies have compared the turbulence estimated from the Thorpe analysis with the turbulence derived from other methods. There have been studies comparing turbulence from radiosondes with turbulence from radar (Hoshino et al., 2016; Kantha & Hocking, 2011; Kohma et al., 2019; Li et al., 2016; Luce et al., 2014; Wilson et al., 2014). Schneider et al. (2015) calculated turbulence from radiosondes and from

an instrument called the Leibniz Institute of Turbulence Observations in the Stratosphere (LITOS), which had an 8-kHz sampling frequency and compared the two turbulence distributions. Fritts et al. (2016) conducted direct numerical simulations (DNSs) to compare the magnitude of turbulence parameters according to the instability stage and turbulence initiation instability mechanism. Balsley et al. (2018) measured the turbulence using a small air vehicle called a DataHawk unmanned aerial system, which ascends and descends within an altitude range of  $z = 50\text{--}400$  m, and they compared the results with the DNS results.

Wilson et al. (2010, 2011) showed that false turbulent layers can be inferred due to instrumental noise when using Thorpe analysis and suggested a statistical method for identifying those false turbulence layers by considering background stability and instrumental noise level. In addition, Wilson et al. (2013) showed that the turbulence strength can be increased due to decreased stability by the latent heat release when the vertical displacement of the air parcel occurred in a moist saturated layer, and they applied dry and saturated buoyancy frequencies to construct potential temperature profiles.

Although several studies have used the Thorpe analysis to estimate the turbulence from various radiosonde observations, little information was available about the spatial distribution of turbulence because those previous studies were based on campaign observations in limited areas. In this study, we investigate the distribution and long-term variability of the turbulence over a much wider spatiotemporal range using data from 68 operational stations in the U.S. mainland for 4 years from September 2012 to August 2016. In addition, the same analysis is conducted at four stations where more than 10-year data (October 2005 to September 2017) are available.

This paper is organized as follows. HVRRD are introduced in section 2. The Thorpe analysis, which is a method for detecting and estimating turbulence from HVRRD, is described in section 3. In section 4, the spatiotemporal distribution and long-term variability of turbulence are shown. Discussion of the results is presented in section 5, and summary and conclusions are presented in section 6.

## 2. Data

In this study, we used 1-s-resolution operational radiosonde data, known as HVRRD, based on radiosondes launched twice a day in the United States at 00 and 12 UTC since 2005. The vertical resolution is approximately 5 m, considering the average radiosonde ascent speed (5.2 m/s). The HVRRD include atmospheric pressure, temperature, horizontal wind speed, RH, latitude, longitude, and altitude data. Figure 1 shows the locations of U.S. mainland radiosonde stations providing HVRRD (Figure 1a), as well as the periods of operation for each station (Figure 1b). In this study, we used data from 68 operational stations located in the U.S. mainland, and the locations of stations are represented as a station index in Figure 1a. The station index is a number ordered from high to low latitudes. Table A1 gives station information, such as the World Meteorological Organization identification, name, latitude, and longitude. As shown in Figure 1b, the starting date of HVRRD differs for each station. In this study, two analysis periods are collected. The first period is 4 years from September 2012 to August 2016, shaded in yellow in Figure 1b, where HVRRD are available at all 68 stations. The number of radiosonde profiles during this period is 183,313. The second period, marked in red in Figure 1b, is more than 10 years at four stations among the 68 stations where long-period data are available: 12 years between October 2005 and September 2017 at the Minneapolis, Salt Lake City, and Corpus Christi stations and 11 years between October 2005 and September 2016 at Sterling station. The number of radiosonde profiles during this period is 31,900. The HVRRD were downloaded from the Stratosphere-troposphere Processes And their Role in Climate Data Centre at Stony Brook University, NY, USA (available online at <http://www.sparc-climate.org/data-center/data-access/us-radiosonde>) and the National Oceanic and Atmospheric Administration (available online at <ftp://ftp.ncdc.noaa.gov/pub/data/ua/rrs-data/>). The HVRRD data downloaded are the “processed data” for which general quality control has been applied. In this study, profiles without RH data and those with a maximum altitude of less than 5 km are excluded.

Figure 2 shows the radiosonde drifting trajectories for 4 years (September 2012 to August 2016). The radiosondes mainly drifted to the east, and the trajectory spreads further in the eastern United States than in the western United States. The mean horizontal distance traveled before the balloon burst was approximately 79 km, and this is a reasonable horizontal distance to have at a midlatitude stations (Kantha & Hocking, 2011; Luce et al., 2014). Since radiosondes can reach a mean altitude of 33 km, it is possible to estimate turbulence in the entire troposphere and in the lower stratosphere. Except for four stations (Nos. 39, 41, 49, and 50),

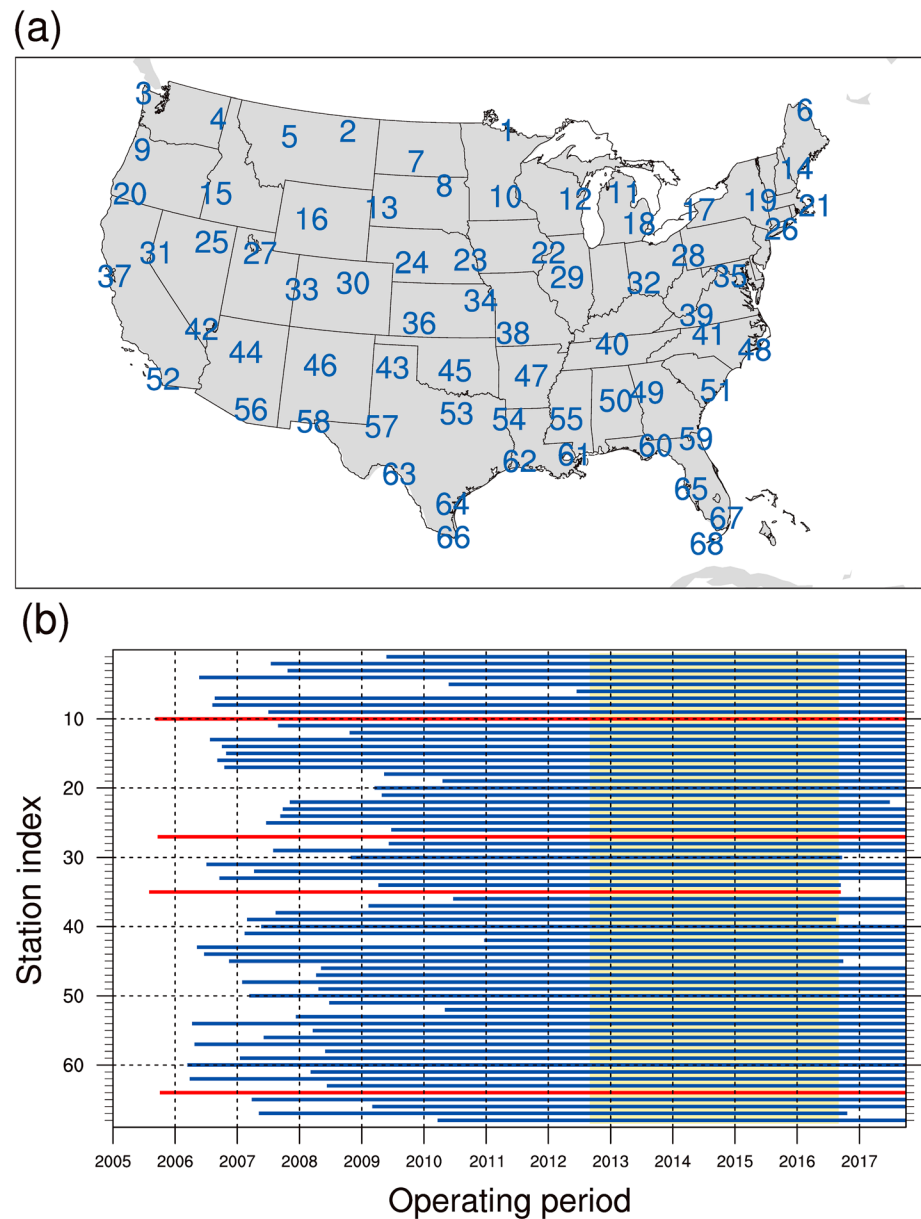


**Figure 1.** (a) Locations and station indices of 68 radiosonde stations used in this study and (b) operating period of each station. In (b), the data period used in this study is shaded in yellow (September 2012 to August 2016) and marked in red (October 2005 to September 2017 for station indices 10, 27, and 64; October 2005 to September 2016 for station index 35). The information of each station is described in Table A1.

there are no overlaps in the trajectories, so that turbulence at each station can represent nearby values rather than being representative of other stations.

### 3. Methods

We calculate potential temperature  $\theta$  (K) using atmospheric pressure  $P$  (hPa) and temperature  $T$  (K) provided for each altitude in HVRRD:  $\theta = T(1,000/P)^{R/c_p}$ , where  $R$  is the specific gas constant for dry air and  $c_p$  is the specific heat capacity. If the atmosphere is stably stratified,  $\theta$  has a positive gradient with respect to altitude. If there is an altitude region with a negative  $\theta$  gradient, this corresponds to an unstable layer. In this study, following Thorpe (1977), we detected unstable layers and inferred the turbulence by re-sorting the observed  $\theta$  profile to a monotonically increasing profile, assuming that the unstable layers were originally

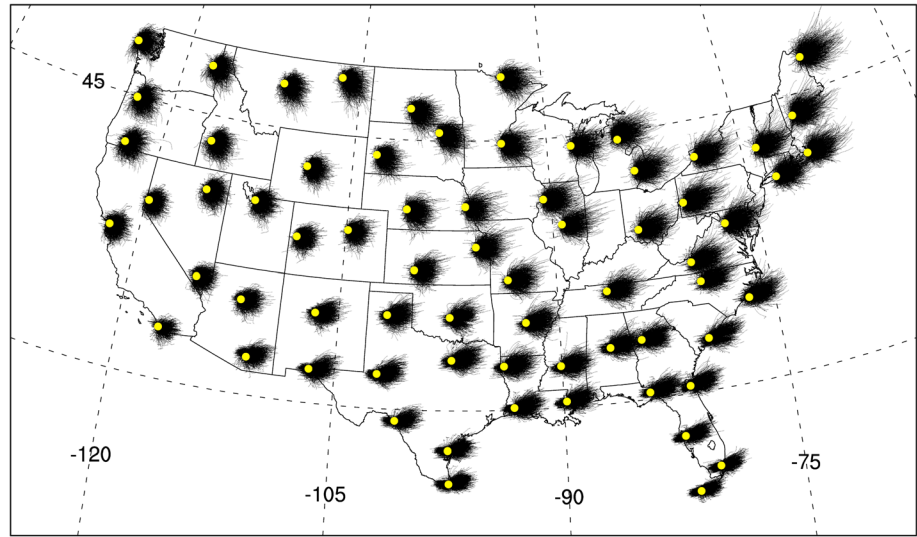


**Figure 2.** All radiosonde drifting trajectories for 4 years (September 2012 to August 2016) at each station. Yellow dots indicate the locations of radiosonde stations. Collective plots of all radiosonde trajectories are shown surrounding each station.

induced by turbulent motions in the vertical direction. The HVRD used in this study have 1-s resolution, but, because the ascent speed of the radiosonde is not constant, the vertical resolution of the profile is not constant. Therefore, the observed pressure, temperature, and RH data are regridded to 5-m intervals using cubic-spline interpolation before the Thorpe analysis is performed.

Although  $\theta$  can be obtained from the observed pressure and temperature data, it is reconstructed from the buoyancy frequency considering moisture effects. Then, the Thorpe analysis is performed using the reconstructed  $\theta$  (hereafter  $\theta^*$ ). Air has three states, dry, subsaturated, and saturated, but the effect of water vapor is negligible in the subsaturated air; thus, we only considered dry and saturated air as in Wilson et al. (2013). When the vertical displacement of an air parcel occurs in the saturated layer,  $\theta$  is not a conservative quantity due to latent heat release, and the stability is lower than in dry air. Considering this point,  $\theta^*$  can be calculated as (Wilson et al., 2013)

$$\begin{aligned}\theta^*(i) &= \theta^*(i-1) \left[ 1 + N_d^2(i-1) \frac{\Delta z}{g} \right] \text{ for dry air and} \\ \theta^*(i) &= \theta^*(i-1) \left[ 1 + N_m^2(i-1) \frac{\Delta z}{g} \right] \text{ for saturated air,}\end{aligned}\quad (1)$$

where  $i$  is the  $i$ th altitude grid from the bottom,  $g$  is the gravitational acceleration,  $N_d^2(k) = \frac{g}{\theta(k)} \left( \frac{d\theta}{dz} \right)_k$  is the squared dry Brunt-Väisälä frequency, and  $N_m^2(k)$  is the squared moist Brunt-Väisälä frequency, which can be expressed as (Durrant & Klemp, 1982; Lalas & Einaudi, 1974)

$$N_m^2(k) = \frac{g}{T(k)} \left[ \left( \frac{\partial T}{\partial z} \right)_k + \Gamma_m(k) \right] \left[ 1 + \frac{L_V q_S(k)}{RT(k)} \right] - \frac{g}{1 + q_w(k)} \left( \frac{dq_w}{dz} \right)_k. \quad (2)$$

Here  $L_V$  is the latent heat of vaporization of water or ice,  $q_w$  is the total mixing ratio, which is the summation of the mixing ratio of water or ice  $q_L$  and the saturated water vapor mixing ratio  $q_S$ , and  $\Gamma_m(k)$  is the moist saturated lapse rate, which is obtained following Durrant and Klemp (1982) as

$$\Gamma_m(k) = \frac{g}{c_{pd}} [1 + q_w(k)] \times \left[ 1 + \frac{c_{pv} q_S(k) + c_w q_L(k)}{c_{pd}} + \frac{\gamma L_V^2 q_S(k)}{c_{pd} R T^2(k)} \left( 1 + \frac{q_S(k)}{\gamma} \right) \right]^{-1}, \quad (3)$$

where  $c_{pd}$  is the specific heat capacity of dry air,  $c_w$  is the specific heat capacity of water or ice,  $c_{pv}$  is the specific heat capacity for water vapor, and  $\gamma \approx 0.622$ .



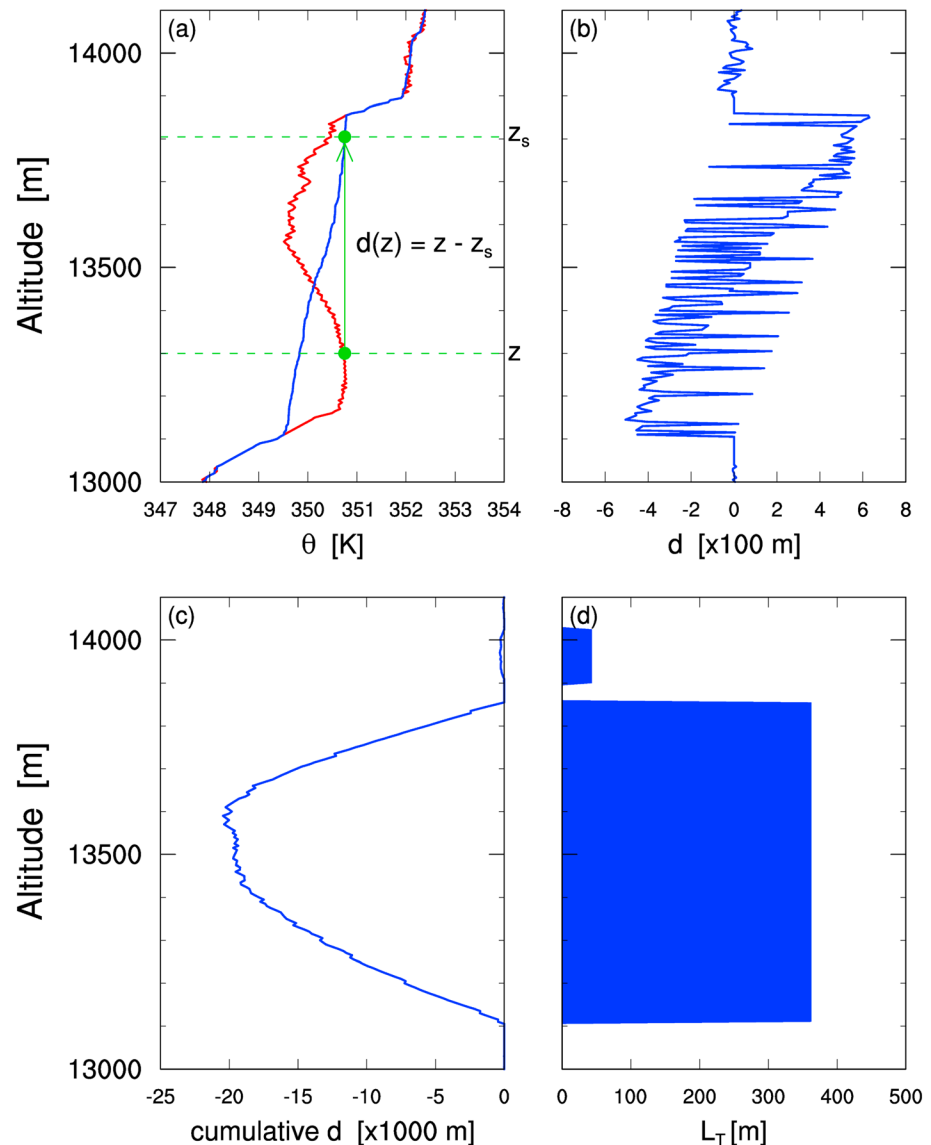
We determined the moist saturated layer based on two empirical thresholds of RH ( $RH_{\max}$  and  $RH_{\min}$ ), which are determined using the RS92 radiosonde data in comparison with W Band (95 GHz) Atmospheric Radiation Measurement Program Cloud Radar (Zhang et al., 2010). The two thresholds vary with altitude:  $RH_{\max}$  ( $RH_{\min}$ ) is decreased from 95% (92%) to 93% (90%) at 0–2 km, from 93% (90%) to 90% (88%) at 2–6 km, from 90% (88%) to 80% (75%) at 6–12 km, and is 80% (75%) above 12 km. If all  $RH \geq RH_{\min}$  within the altitude range of  $z_i - z_j$  and if there is a simultaneous  $k$ th altitude grid where  $RH(k) \geq RH_{\max}$  within the altitude range of  $z_i - z_j$ , then the altitude range  $z_i - z_j$  is determined to be a moist saturated layer. Wilson et al. (2013) and Sunilkumar et al. (2015) have shown that the Thorpe scale ( $L_T$ ) is much larger due to the stability decrease in the results when using  $\theta^*$  rather than  $\theta$  for the turbulent layer.

Figure 3 shows the process of estimating the Thorpe scale from the  $\theta^*$  profile. First, we construct a re-sorted  $\theta^*$  (hereafter  $\tilde{\theta}^*$ ) profile by vertically aligning the  $\theta^*$  for a monotonic increase with increasing altitude. The red line in Figure 3a shows the observed  $\theta^*$  profile, and the blue line shows the  $\tilde{\theta}^*$  profile. If  $\theta^*$  at an arbitrary altitude  $z$  is located at the altitude  $z_s$  in the  $\tilde{\theta}^*$  profile, this can be thought of as the  $\theta^*$  being moved by  $z - z_s$  from the  $\tilde{\theta}^*$  profile by overturning. From this result, the Thorpe displacement is defined as  $d(z) = z - z_s$ , which is shown in Figure 3b. When making a  $\tilde{\theta}^*$  profile from the  $\theta^*$  profile, if a displacement occurs at an arbitrary altitude grid, this means that the displacement in the opposite direction must occur at some other point. Therefore, in Figure 3c, when integrating  $d(z)$  upward from  $z_m$  where  $d(z) > 0$  appears and then the integral value equals 0 at  $z_n$ , that is, if  $\sum_{i=m}^{i=n} d(z_i) = 0$ , we determine  $z_m - z_n$  as the turbulent layer (Wilson et al., 2010). The root-mean-square value of the  $d(z)$  in each turbulent layer is called the Thorpe scale  $L_T$ , as shown in Figure 3d.  $L_T$  represents the local overturning scale, and Thorpe (1977) assumed a linear relationship between  $L_T$  and the Ozmidov scale  $L_O = (\varepsilon/N^3)^{1/2}$  (Ozmidov, 1965), where  $\varepsilon$  is the turbulent kinetic energy (TKE) dissipation rate or eddy dissipation rate. That is, by letting  $L_O = cL_T$  ( $c$  is an empirical constant), a relation between  $\varepsilon$  and  $L_T$  can be derived as follows:

$$\varepsilon = C_K L_T^2 N^3, \quad (4)$$

where  $C_K = c^2$ . Here  $N$  is the Brunt-Väisälä frequency of a stably stratified atmosphere and is therefore calculated from the  $\tilde{\theta}^*$  profile (Clayson & Kantha, 2008; Dillon, 1982; Muhsin et al., 2016; Sorbján & Balsley, 2008; Thorpe, 2005). In this study, following Kantha and Hocking (2011) and Li et al. (2016), who performed a statistical comparison of HVRD-derived  $\varepsilon$  with radar-derived  $\varepsilon$ , we set  $C_K = 1.0$ . Uncertainty in  $C_K$  introduces a corresponding uncertainty in  $\varepsilon$ . A more detailed discussions about  $C_K$  will be presented in section 5.2.

Instrumental noise is an important issue when estimating turbulence from observational data. As mentioned earlier, Wilson et al. (2010, 2011) presented a method of statistically identifying false turbulent layers induced by instrumental noise. In this study, we briefly introduce this method. First, the variance of the instrumental noise can be obtained as half of the average variance of each of the five successive data grids after eliminating the linear trend; then, the standard deviation of the instrumental noise  $\sigma_N$  can be obtained. In this study,  $\sigma_N$  for  $\theta^*$  is calculated as  $2.51 \times 10^{-2}$  (K), and this value is consistent with those in Bellenger et al. (2017), Figure 2b). The bulk-tnr (trend to noise ratio) can be obtained by dividing the range of  $\theta^*$  by  $\sigma_N$ . This bulk-tnr is an indicator of the background atmosphere stability relative to the instrumental noise. Generally, the lower the bulk-tnr, the higher the probability of a false turbulent layer. Therefore, if the bulk-tnr is too small (generally less than 0.80), an additional noise reduction process is required. The mean bulk-tnr of the current study is 0.83 and 5.60 in the troposphere and stratosphere, respectively. Because the bulk-tnr value of 0.83 in the troposphere is larger than 0.80, which is the minimum bulk-tnr in previous studies (Kantha & Hocking, 2011; Muhsin et al., 2016; Sun et al., 2016; Sunilkumar et al., 2015), an additional noise reduction process is not performed. The minimum detectable size of the turbulent layer can be obtained from the bulk-tnr in the troposphere and stratosphere of the individual profiles (Wilson et al., 2010, Figure 5), and only turbulent layers with sizes larger than this minimum detectable size are selected as the true turbulent layers. In addition, turbulent layers with a range of  $\theta^*$  exceed the 99% confidence level are selected exclusively as the true turbulent layers (Bellenger et al., 2015; Wilson et al., 2010). As a result, the ratio of turbulent layers decreased from



**Figure 3.** The Thorpe analysis process. (a) Observed (red) and re-sorted (blue) profiles of reconstructed potential temperature, (b) Thorpe displacement, (c) cumulative Thorpe displacement, and (d) Thorpe scale.

66% to 44% and from 15% to 12% in the troposphere and stratosphere, respectively, after considering the instrumental noise.

Given that the Thorpe analysis cannot distinguish between convectively induced turbulence (CIT) and shear-induced turbulence (SIT; Thorpe, 2005), the turbulence can be overestimated near the surface during the daytime. With this in mind, for example, Sun et al. (2016) calculated the turbulence in the boundary layer only for nighttime. In order to use all profiles launched both in daytime and nighttime, in the present study, we show  $L_T$  and  $\epsilon$  exclusively in the free atmosphere, from 3 km above the station height to the top of the radiosonde profile. A related discussion will be presented in section 5.1.

## 4. Results

### 4.1. Vertical Distribution of Turbulence

Figure 4 shows a sample profile derived from radiosonde data at the Bismarck station (station index 7 in Figure 1) in North Dakota, USA, at 00 UTC on 10 August 2016. The dashed line in each figure indicates

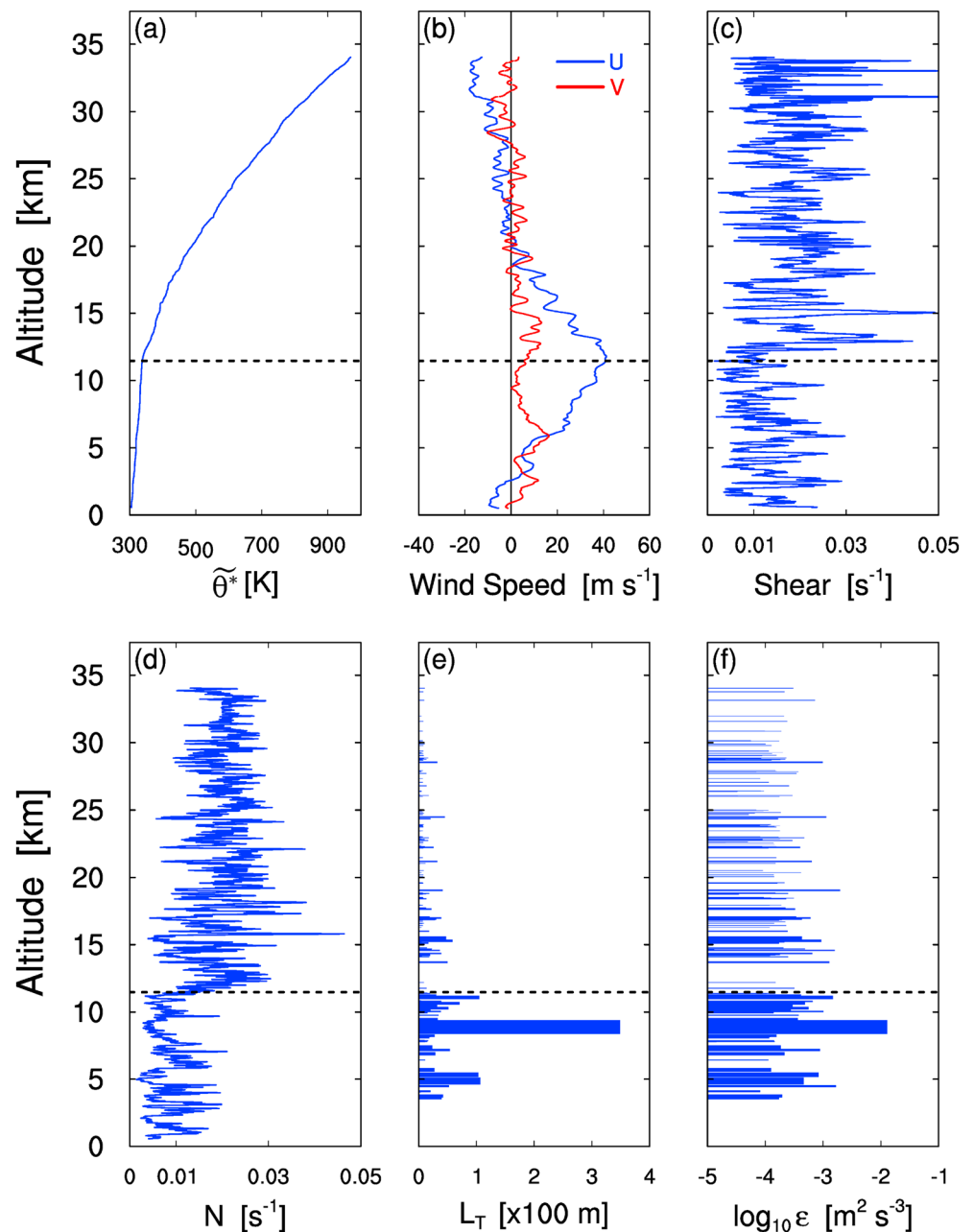


**Figure 4.** Vertical profiles retrieved from high vertical-resolution radiosonde data at Bismarck station (46.77°N, 100.75°W), ND, USA, on 00 UTC 10 August 2016: (a) re-sorted reconstructed potential temperature, (b) horizontal wind speed (U: blue and V: red), (c) vertical wind shear, (d) Brunt-Väisälä frequency, (e) Thorpe scale, and (f) eddy dissipation rate. The dashed line in each plot represents the tropopause height. Note that only data 3 km above the station height and higher are shown in (e) and (f). For better representation, vertical wind shear in (c) and Brunt-Väisälä frequency in (d) are smoothed by a 21-point (100 m) running mean filter.

the altitude of the first tropopause defined by World Meteorological Organization (1957), which is “the lowest level at which the lapse rate decreases to 2 ° C/km or less, provided also the average lapse rate between this level and all higher levels within 2 km does not exceed 2 ° C/km.” Figure 4a shows the  $\tilde{\theta}^*$  profile in the troposphere and stratosphere. In Figure 4b, the horizontal wind speed in the troposphere gradually increases with increasing altitude, and the zonal wind ( $U$ ) is larger than the meridional wind ( $V$ ). Wind speed is at its maximum near the tropopause and gradually decreases as the altitude increases in the stratosphere. The vertical wind shear (VWS) in Figure 4c is calculated from the horizontal wind



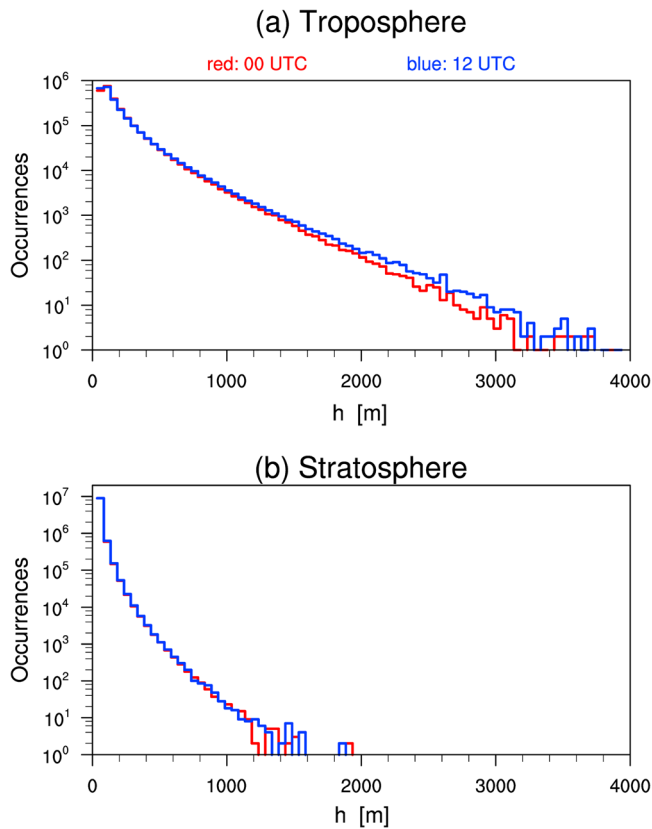


**Figure 5.** Histogram of turbulent layer thickness ( $h$ ) for 4 years (September 2012 to August 2016) in the (a) troposphere (from 3 km above the station height to the tropopause) and (b) stratosphere (from the tropopause to  $z = 33$  km). Red and blue indicate data for 00 and 12 UTC, respectively.

the VWS is very large, turbulent layers are seldom found. The gradient Richardson number is greater than 0.25 in almost all altitude regions for  $z = 12$ – $13$  km (not shown). In this altitude region, turbulence may be suppressed due to the rapid stability increase (Obukhov, 1971). In the stratosphere, many thin and weak turbulent layers appear, relative to those in the troposphere.

Figure 5 shows the distribution of turbulent layer thickness ( $h$ ) for 4 years (September 2012 to August 2016) in the troposphere (from 3 km above the station height to the tropopause) and stratosphere (from the tropopause to  $z = 33$  km). Red and blue indicate data for 00 and 12 UTC, respectively. In this figure, all  $h$  are thicknesses of true turbulent layers considering instrumental noise (Wilson et al., 2010, 2011). A total of  $2.93 \times 10^7$  ( $5.14 \times 10^7$ ) turbulent layers are detected, and  $5.09 \times 10^6$  ( $2.06 \times 10^7$ ) turbulent layers are selected as true turbulent layers in the troposphere (stratosphere). The numbers of  $h$  for 00 and 12 UTC are almost the same. The mean (median) value of  $h$  is 159 m (100 m) and 23 m (10 m) in the troposphere and stratosphere, respectively. The 95th percentile value of  $h$  is 495 and 75 m in the troposphere and stratosphere, respectively. In the troposphere, the proportion of large  $h$  is much higher than in the stratosphere. Therefore, a relatively small proportion of large  $h$  in the stratosphere is likely due to stronger stability.

The distribution of  $h$  was also shown in some previous studies (e.g., Bellenger et al., 2017; Wilson et al., 2018). Using about 3,500 radiosonde soundings over the Indian Ocean, Bellenger et al. (2017), Figure 4a) presented the distribution of  $h$  in the troposphere. They showed that occurrence of  $h$  monotonically decreases with increasing  $h$ , which is consistent with the present result in the troposphere (Figure 5a). Using about 110 radiosonde soundings at the Shigaraki observatory ( $34^{\circ}51'N$ ,  $136^{\circ}06'E$ ) in Japan, Wilson et al. (2018), Figure 4) showed that the distribution of  $h$  follows a power law. When Figure 5 of the present study is plotted on log-log plot (not shown), the results do not follow a power law in both the troposphere and stratosphere. As noted in Wilson et al. (2018), the power law of the distribution of  $h$  does not seem to be universal. Given

speed:  $\left( \sqrt{(\partial U / \partial z)^2 + (\partial V / \partial z)^2} \right)$ . We set the vertical interval  $z = 5$  m for computing VWS, but for better representation, Figure 4c shows a smoothed profile using a 21-point moving average. Note that this smoothing was only performed for display, and the nonsmoothed VWS was used in other calculations. The Brunt-Väisälä frequency  $N$  (Figure 4d) is calculated from  $\tilde{\theta}^*$  (Figure 4a). Similar to VWS, the  $N$  profile in Figure 4d is smoothed using a 21-point moving average. This smoothing was only performed for display, and the nonsmoothed  $N$  was used to calculate  $\epsilon$ . In the troposphere,  $N$  fluctuates around a mean value of  $0.01 \text{ s}^{-1}$  and increases rapidly while passing through the tropopause, while in the stratosphere,  $N$  fluctuates around its approximate mean value of  $0.02 \text{ s}^{-1}$ . In this profile, moist saturated layers are found at  $z = 5,710$ – $5,845$  m,  $5,955$ – $7,060$  m, and  $8,315$ – $8,815$  m, and the corresponding mean  $N$  of these three layers decreased from  $7.66 \times 10^{-3} \text{ s}^{-1}$  to  $7.65 \times 10^{-3} \text{ s}^{-1}$ , from  $1.11 \times 10^{-2} \text{ s}^{-1}$  to  $1.10 \times 10^{-2} \text{ s}^{-1}$ , and from  $5.96 \times 10^{-3} \text{ s}^{-1}$  to  $5.71 \times 10^{-3} \text{ s}^{-1}$ , respectively, after considering the moist saturation effect. The Thorpe scale  $L_T$  in Figure 4e shows only the significant turbulent layers determined as in Wilson et al. (2010, 2011). Finally, Figure 4f shows  $\epsilon$  calculated from equation (4).

In Figures 4e and 4f, there are thicker and stronger turbulent layers in the troposphere than in the stratosphere, and the troposphere is mostly filled with turbulent layers. The thickest turbulent layer appears at  $z = 8.5$ – $9.5$  km, where the altitude region corresponds well to the low-stability region in Figure 4d. Additionally, at  $z = 4.5$ – $5.5$  km, thick turbulent layers appear and correspond to low-stability regions. Most of the turbulent layers are clustered in groups of more than two or three, and similar results are often found in previous studies (e.g., Kantha & Hocking, 2011; Luce et al., 2014; Schneider et al., 2015; Sunilkumar et al., 2015; Wilson et al., 2010; Wilson et al., 2013). In Figure 4c at  $z = 12$ – $13$  km above the tropopause, although

that the thick turbulent layers are likely associated with convection (discussed later in section 5.1), we have additionally calculated the distribution of  $h$  containing moist saturated layer exclusively. The results for the moist saturated layers are almost the same as in Figure 5 (not shown).

Although we mainly focused on  $\epsilon$  throughout this study, there are some implications from the current results to model the effective diffusivity  $K$ , which is important for mixing and dispersion of trace gases and pollutants, especially in strongly stratified regions such as in the stratosphere. Dewan (1981), assuming intermittency and random altitudes of turbulent layer, investigated  $K$  by performing numerical simulation for various boundary and initial conditions. Dewan (1981) showed that  $K$  depends on the frequency of occurrence of turbulence and turbulent layer thickness  $h$ . Vanneste and Haynes (2000) designed Dewan's (1981) model more rigorously and extended it for more general cases. Osman et al. (2016) performed a  $K$  modeling, coupled with observational data and showed that a small number of thick turbulent layers dominate the mixing rather than a large number of thin turbulent layers. In these studies, the most important factor in determining  $K$  is the distribution of  $h$ . To the author's knowledge, there have been no previous studies showing the distribution of  $h$  in the stratosphere over a wide geographical range and for a long period as in the present study, and thus, the result in Figure 5b can provide reliable information on the distribution of  $h$  in the stratosphere. It is our hope that the results in this paper will be useful for further exploring mixing in the predominantly stable stratosphere where intermittent turbulent layers occur.

Figures 6a and 6b show the percent distribution of  $\log_{10}\epsilon$ ,  $L_T$  and  $N$  from the HVRRD of 68 stations for 4 years from September 2012 to August 2016 in the troposphere (from 3 km above the station height to the tropopause) and in the stratosphere (from the tropopause to  $z = 33$  km), respectively. The red and blue indicate the result for 00 UTC and 12 UTC, respectively, as in Figure 5. Dashed lines in the upper plot show the lognormal distribution using 5th to 95th percentile data. The range of  $\log_{10}\epsilon$  is from  $-5$  to  $-2$  ( $\epsilon$  being in square meters per cubic second). The mean value of  $\log_{10}\epsilon$ , indicated as a middle dashed vertical line, is  $-3.735$  ( $\epsilon = 1.84 \times 10^{-4} \text{ m}^2/\text{s}^3$ ) and  $-3.862$  ( $\epsilon = 1.37 \times 10^{-4} \text{ m}^2/\text{s}^3$ ) in the troposphere and stratosphere, respectively. This means that the turbulent layers in the stratosphere are relatively weaker than in the troposphere. This can also be seen in the results of  $L_T$  (Figure 6, middle), which has a much broader distribution in the troposphere than in the stratosphere. The mean values of  $L_T$  are 28 and 10 m in the troposphere and stratosphere, respectively. As might be expected from the  $N$  results (Figure 6, lower), it seems that a much smaller  $L_T$  is seen in the stable stratosphere than in the troposphere. The mean value of  $N$  is  $0.008 \text{ s}^{-1}$  in the troposphere and  $0.012 \text{ s}^{-1}$  in the stratosphere, which is smaller than the generally accepted values of 0.01 and  $0.02 \text{ s}^{-1}$ , respectively. This is because only the  $N$  values within the turbulent layers, where  $L_T > 0$ , are used for the calculation. These results are consistent with the results of Bellenger et al. (2017), Figure 6) and Wilson et al. (2018), Figure 5), who examined the distribution of  $N$  both within and outside of turbulent layers. The larger  $\epsilon$  in the troposphere than in the stratosphere result from the larger  $L_T$  overcoming the smaller  $N$ . In the troposphere, the distribution of  $\epsilon$  is approximately lognormal with a positive skewness, but in the stratosphere, the distribution of  $\epsilon$  has three modes. Recalling that  $\epsilon$  estimates depend on  $L_T$  and  $N$  (equation (4)), three local maxima in the  $\epsilon$  distribution might occur because the distribution of  $N$  has three modes. The three-mode structure of  $N$  in the stratosphere is robust for all seasons (not shown). The origin of these three modes remains open.

Lindborg (1999) estimated a mean value of  $\epsilon = 7.64 \times 10^{-5} \text{ m}^2/\text{s}^3$  at  $z = 10$  km, whereas Frehlich and Sharman (2010) obtained a mean value of  $\epsilon = 5.2 \times 10^{-5} \text{ m}^2/\text{s}^3$  at  $z = 10$  km. Cho and Lindborg (2001) estimated a mean value of  $\epsilon = 6 \times 10^{-5} \text{ m}^2/\text{s}^3$  in the stratosphere. These values are slightly smaller than that in this study, but the difference is within a factor of 2–4. Relatively large value of  $\epsilon$  in the present study based on the Thorpe method is partially because commercial aircrafts tend to avoid forecasted strong turbulent regions as mentioned by Sharman et al. (2014), along with different methods used to calculate the eddy dissipation rate.

Dehghan et al. (2014) and Hocking and Mu (1997) showed the complementary cumulative distribution of  $\epsilon$  and discussed the probability of  $\epsilon$  exceeding  $10^{-3} \text{ m}^2/\text{s}^3$ . When Figure 6 is replotted (not shown) in the complementary cumulative form, the probability of  $\epsilon$  exceeding  $10^{-3} \text{ m}^2/\text{s}^3$  is 2.1% at 00 UTC and 1.8% at 12 UTC in the troposphere. This implies that the “light-or-greater” turbulence, classified as  $\epsilon^{1/3} > 0.1 \text{ m}^{2/3}/\text{s}$  by the International Civil Aviation Organization (2016), is rare. This is consistent with Dehghan et al. (2014), Figure 11c), who showed the probability of  $\epsilon$  exceeding  $10^{-3} \text{ m}^2/\text{s}^3$  being 2% from both aircraft and radar measurements. On the other hand, Hocking and Mu (1997), Figure 14) showed that the probability of  $\epsilon$

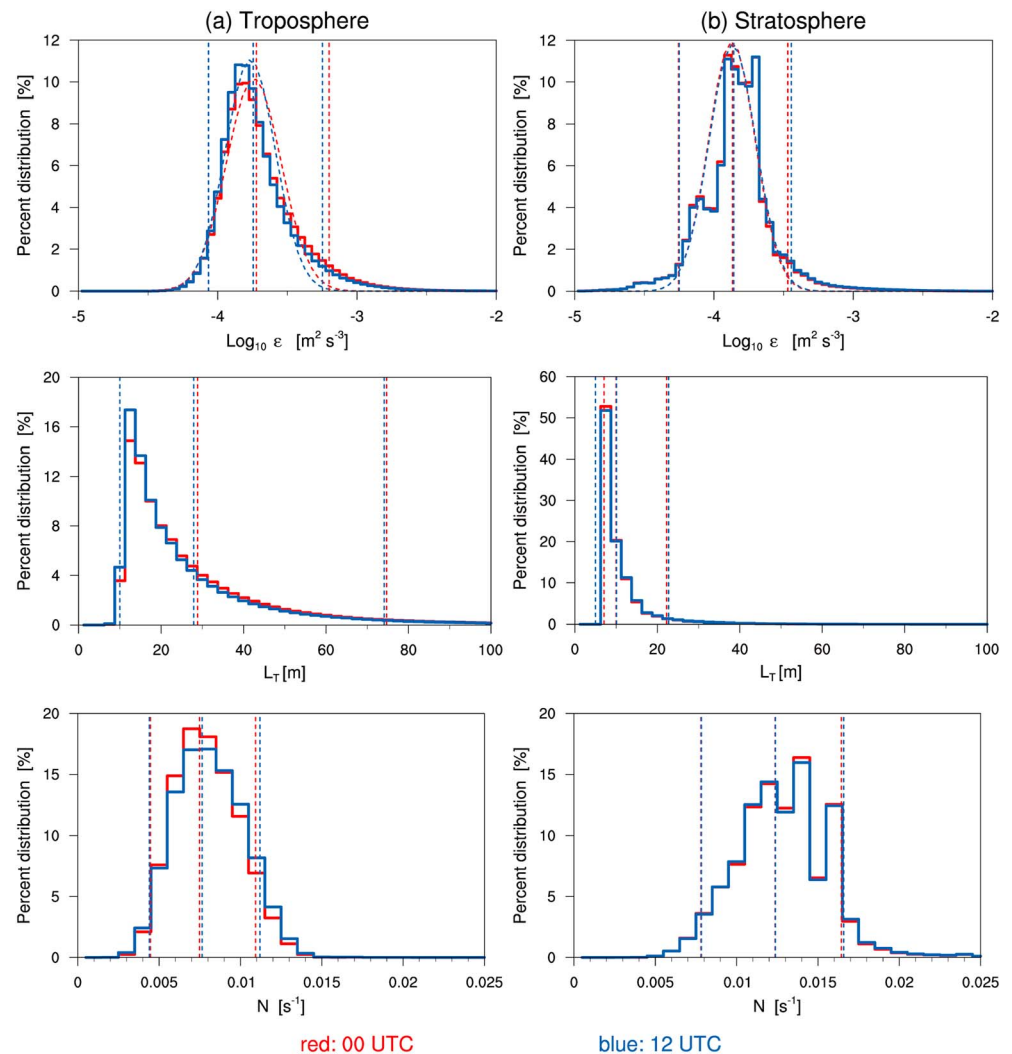


**Figure 6.** (solid line) Percent distribution of logarithmic eddy dissipation rate ( $\log_{10}\epsilon$ ), Thorpe scale ( $L_T$ ), and Brunt-Väisälä frequency ( $N$ ) for 4 years (September 2012 to August 2016) in the (a) troposphere (from 3 km above the station height to the tropopause) and (b) stratosphere (from the tropopause to  $z = 33$  km). Vertical dashed lines show the (left) 5th percentile, (middle) mean, and (right) 95th percentile values for all data. Red and blue represent the data for 00 and 12 UTC, respectively. Dashed lines in upper plot show the lognormal distribution using 5th to 95th percentile data. Note that only the  $N$  within turbulent layers are used in the lower plots.

exceeding  $10^{-3} \text{ m}^2/\text{s}^3$  is about 30%. The large probability may be due to the differences in estimation method of  $\epsilon$  (Dehghan et al., 2014) and/or geographical location.

The 00 and 12 UTC in the U.S. mainland correspond generally to evening (corresponding to 17–20 LT in the continental United States) and morning (corresponding to 05–08 LT in the continental United States), respectively. In the troposphere,  $\log_{10}\epsilon$  and  $L_T$  for 00 UTC (red) are larger than those for 12 UTC (blue), although  $N$  is the opposite. This is somewhat expected in the sense that stronger turbulence will occur due to low stability during the evening. In the stratosphere, however,  $\log_{10}\epsilon$  and  $L_T$  during the evening are slightly smaller than those during the morning, although the differences in  $\log_{10}\epsilon$  and  $L_T$  between 00 and 12 UTC are relatively smaller than those in the troposphere. In the troposphere and stratosphere, the difference between the distribution of  $\log_{10}\epsilon$  during the evening and morning is statistically significant using both the  $t$  test and Kolmogorov-Smirnov test at the 99% confidence level. Interestingly, the turbulent layer thickness  $h$  is larger during the morning than evening (Figure 5), although  $\log_{10}\epsilon$  is the opposite. This implies that the overturning appears in a deeper layer during the morning, likely including more small-scale turbulent eddies resulting in smaller  $\log_{10}\epsilon$  and  $L_T$  in the morning.

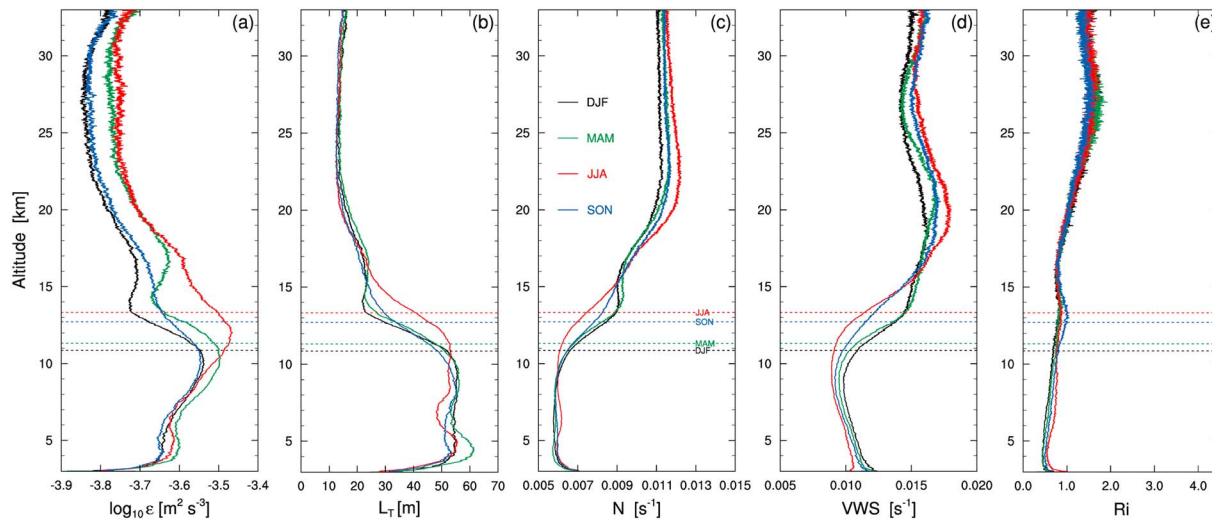


**Figure 7.** Vertical profiles of the seasonal mean of (a) logarithmic eddy dissipation rate ( $\log_{10}\epsilon$ ), (b) Thorpe scale ( $L_T$ ), (c) Brunt-Väisälä frequency ( $N$ ), (d) vertical wind shear, and (e) gradient Richardson number ( $Ri$ ) for 4 years (September 2012 to August 2016). The seasonal mean tropopause height is represented by the horizontal dashed line in each plot. Note that only the  $N$ , vertical wind shear, and  $Ri$  within turbulent layers are used in (c), (d), and (e), respectively. Turbulent layers containing  $z = 3$  km are not used in calculating each mean profile. DJF = December–February; JJA = June–August; MAM = March–May; SON = September–November.

Figure 7 shows the seasonal mean profiles of  $\log_{10}\epsilon$ ,  $L_T$ ,  $N$ , VWS, and gradient Richardson number ( $Ri = N^2/VWS^2$ ), which are calculated from the HVRD of 68 stations for 4 years from September 2012 to August 2016. Note that only the estimates of  $N$ , VWS, and  $Ri$  within turbulent layers are used in Figures 7c–7e, respectively. Note that the re-sorted potential temperature profile is used in the calculation of  $N$  and  $Ri$ , and therefore,  $N^2$  is all positive and  $Ri$  is larger than 0 in Figure 7. Because 5-m-resolution data are used in this study, VWS approaches 0 (even sometimes equal to 0) at some altitude grids, so that  $Ri$  approaches very large values. To make smooth mean profiles, only  $Ri$  less than 100 are used in Figures 7e and S1e. Winter (DJF [December–February]), spring (MAM [March–May]), summer (JJA [June–August]), and autumn (SON [September–November]) are indicated as solid lines of black, green, red, and blue, respectively. The horizontal dashed lines represent the seasonal mean tropopause for those seasons. In the troposphere,  $\log_{10}\epsilon$  increases gradually as the altitude increases, but the value decreases sharply in the vicinity of the tropopause. The largest  $\log_{10}\epsilon$  appeared at approximately 1–2 km below the tropopause during all seasons. In winter and spring (black and green lines),  $\log_{10}\epsilon$  increases slightly in the lower stratosphere and decreases again with increasing altitude, whereas in summer and autumn (red and blue lines),  $\log_{10}\epsilon$  steadily decreases. In the altitude region  $z = 24$ –30 km,  $\log_{10}\epsilon$  is relatively constant during all seasons. Above  $z = 30$  km,  $\log_{10}\epsilon$  increases slightly during all seasons. The largest gradients between 3 and 4 km in the Figure 7a are artificial, because we did not use turbulent layers containing  $z = 3$  km for the calculation. Consistent with the tropopause seasonal variation, the altitude at which  $\log_{10}\epsilon$  is at its maximum is highest in summer and lowest in winter. The maximum value of the seasonal mean  $\log_{10}\epsilon$  is also the largest in summer. This vertical structure of  $\epsilon$  is consistent with that of Clayson and Kantha (2008), Figure 5), in which  $\epsilon$  was calculated using 2-s-resolution radiosonde data. The strongest turbulence below the tropopause is also seen from individual profiles as well, which will be demonstrated in Figure 11a. The height of the maximum  $\epsilon$  in the current study is different from some previous studies using radar data (e.g., Nastrom & Eaton, 1997, 2005) and the recently published results of Kohma et al. (2019), which showed the maximum  $\epsilon$  occurring just above tropopause primarily by the changes in the static stability ( $N$ ) under nearly height-independent TKE around the tropopause. This is different from the current study of which the vertical profile of  $\epsilon$  is determined primarily by  $L_T$  that is generally larger where  $N$  is smaller, as will be shown in Figures 7b and 7c.

In Figure 7b, the vertical structure of  $L_T$  is similar to that of  $\epsilon$ , but there is a difference in that  $L_T$  is relatively flat across much of the troposphere and  $\epsilon$  shows its maximum in the upper troposphere. The vertical structure of  $L_T$  during the winter, which is shown in black, is quite consistent with the results of Love and Geller (2012), who used data from winter 2007 from the Riverton station (station index 16 in Figure 1). When we

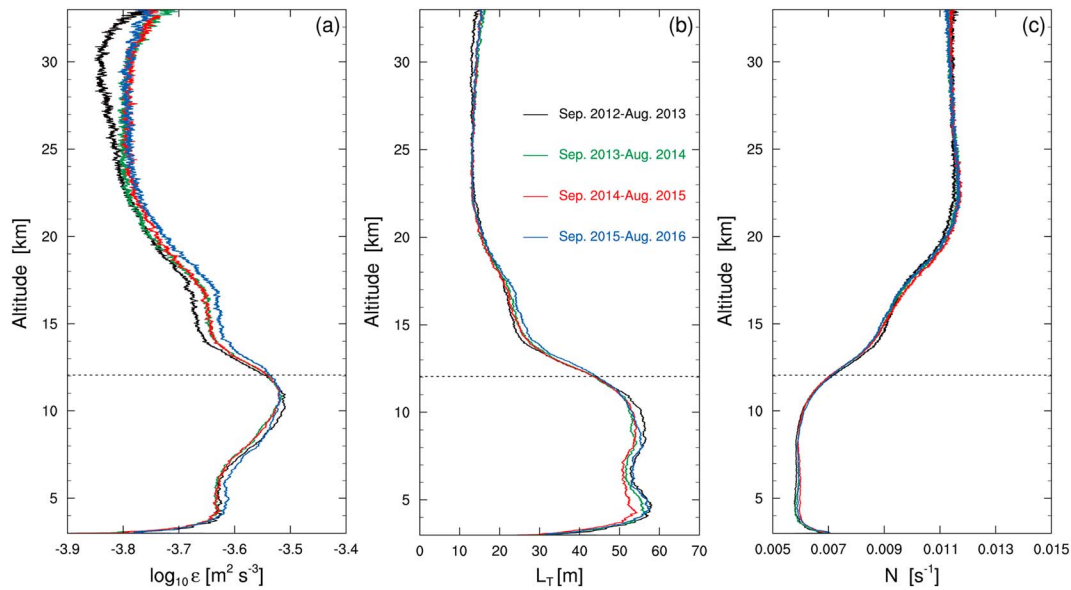


**Figure 8.** Same as Figure 7 but for annual mean profiles. The mean tropopause for 4 years is represented by the horizontal dashed line in each plot.

compare the seasonal mean profiles of  $L_T$  and  $N$ , we can see that there is a negative correlation. It can be considered that  $L_T$  is large (small) because overturning is relatively large (small) in unstable (stable) conditions. Although equation (4) shows that  $\varepsilon$  is proportional to both  $L_T^2$  and  $N^3$ , the vertical structure of  $\varepsilon$  mainly follows that of  $L_T$ , so the influence of  $L_T$  seems to be much greater than  $N$  in determining  $\varepsilon$ . Interestingly, the seasonal variation of  $\varepsilon$  in the troposphere is similar to that of  $L_T$  but is similar to that of  $N$  in the stratosphere. The seasonal variation of  $L_T$  appeared to be small in the stable stratosphere compared to the troposphere, so the seasonal variation of  $\varepsilon$  follows that of  $N$ .

In Figures 7d and 7e, several interesting features are found. First, VWS and Ri are larger in the stratosphere than in the troposphere. In the troposphere, VWS is larger in winter (black) and spring (green) than in other seasons. We found that the mean profile of VWS calculated in turbulent layers is slightly smaller than that calculated in the entire altitude region (see Figure S1d in the supporting information), implying that mixing by turbulence already exists in the turbulent layer. Second, the correlation between  $\varepsilon$  and VWS is not significant, which will be shown in Figure 12 as well. A detailed discussion about the correlation between  $\varepsilon$  and VWS will be given in section 5.3. Third, in Figure 7e, the mean profile of Ri calculated in turbulent layers is much smaller than the mean profile of Ri calculated in the entire altitude region (Figure S1e), because  $N$  is much smaller in turbulent layers than that in the entire altitude region. This is consistent with the work by Bellenger et al. (2017), who showed that  $N$  and Ri are much smaller inside turbulent layers, as determined using data from about 3,500 radiosonde soundings over the Indian Ocean. There is no altitude where the averaged Ri is less than 0.25 in the averaged profile of Ri (Figure 7e), because there are relative few cases for turbulence events with Ri less than 0.25 (18% in the troposphere and 21% in the stratosphere).

Figure 8 shows the annual mean profile of  $\log_{10}\varepsilon$ ,  $L_T$ , and  $N$  in each year during the 4 years calculated from the same data used in Figure 7. The vertical trend of  $\varepsilon$ ,  $L_T$ , and  $N$  is similar to that of Figure 7.  $\varepsilon$  gradually increases with increasing altitude in the troposphere, and the maximum  $\varepsilon$  appears in the upper troposphere and decreases sharply with increasing altitude above the tropopause. In the altitude region  $z = 14$ – $17$  km,  $\varepsilon$  decreases slowly and then tends to decrease rapidly again. Except for the first year (September 2012 to August 2013), there is a nearly constant  $\varepsilon$  in the altitude region  $z = 24$ – $30$  km. In the altitude region  $z = 30$ – $33$  km,  $\varepsilon$  tends to increase in all years. The interannual variation is smaller than the seasonal variation (Figure 7). Although the interannual variation in the altitude region  $z = 14$ – $17$  km is large relative to other altitude regions, the interannual variation in this altitude region is also much smaller than the seasonal variation. In the altitude region  $z = 24$ – $30$  km, turbulence in the first year (black line) is slightly smaller than the turbulence in other years consistent with  $L_T$  being smaller than in the other years. Since the vertical structure of  $L_T$  is similar to that of  $\varepsilon$  except in the lower troposphere,  $\varepsilon$  mainly follows the structure of  $L_T$ . As



shown in Figure 7,  $L_T$  and  $N$  are negatively correlated in the annual profiles. Relationships between some interannual variations, such as El Niño–Southern Oscillation and quasi-biennial oscillation, and turbulence intensity at different seasons and locations need to be investigated further once longer data are available and also for other radiosonde locations.

#### 4.2. Horizontal Distribution of Turbulence

In this section, we examine the horizontal distribution of  $\epsilon$ ,  $L_T$ , and  $N$ . As described in Figure 2, since there are few overlaps between the radiosonde trajectories at each station, it is possible to analyze the horizontal distribution of the turbulence by setting the station locations as the grid points. Based on this idea, the horizontal distributions of  $\epsilon$ ,  $L_T$ , and  $N$  averaged over 4 years (from September 2012 to August 2016) in the troposphere (from 3 km above the station height to the tropopause) and stratosphere (from the tropopause to  $z = 33$  km) are shown in Figures 9b and 9c, respectively. Note that  $\epsilon$  is expressed in a logarithmic scale and  $\epsilon$  is calculated from the product of  $L_T^2$  and  $N^3$  in equation (4). Therefore,  $L_T$  and  $N$  in Figures 9b and 9c are expressed as  $\log_{10} L_T^2$  and  $\log_{10} N^3$ , respectively. Figure 9a shows the terrain height provided from European Centre for Medium-Range Weather Forecasts Reanalysis Interim data ( $0.125^\circ \times 0.125^\circ$ ; Dee et al., 2011). In the troposphere,  $\epsilon$  is large in the western United States, and this pattern is consistent with the terrain height pattern. With this pattern, the large  $\epsilon$  in the troposphere calculated from the Thorpe analysis seems to be related to mountains. Wolff and Sharman (2008), Figure 8) investigated the horizontal distribution of moderate-or-greater mountain wave turbulence above 5.5 km from pilot report data collected over 12 years. They found that even at high altitudes, the horizontal distribution of moderate-or-greater mountain wave turbulence is similar to the mountainous pattern in the western United States. The strongest  $\epsilon$  is revealed at the Flagstaff station (station index 44) located in southwestern United States, but the turbulence in this region cannot be compared to that by Wolff and Sharman (2008), due to the small number of pilot reports in Arizona where air traffic is prohibited for military operations (Figure 2b therein).

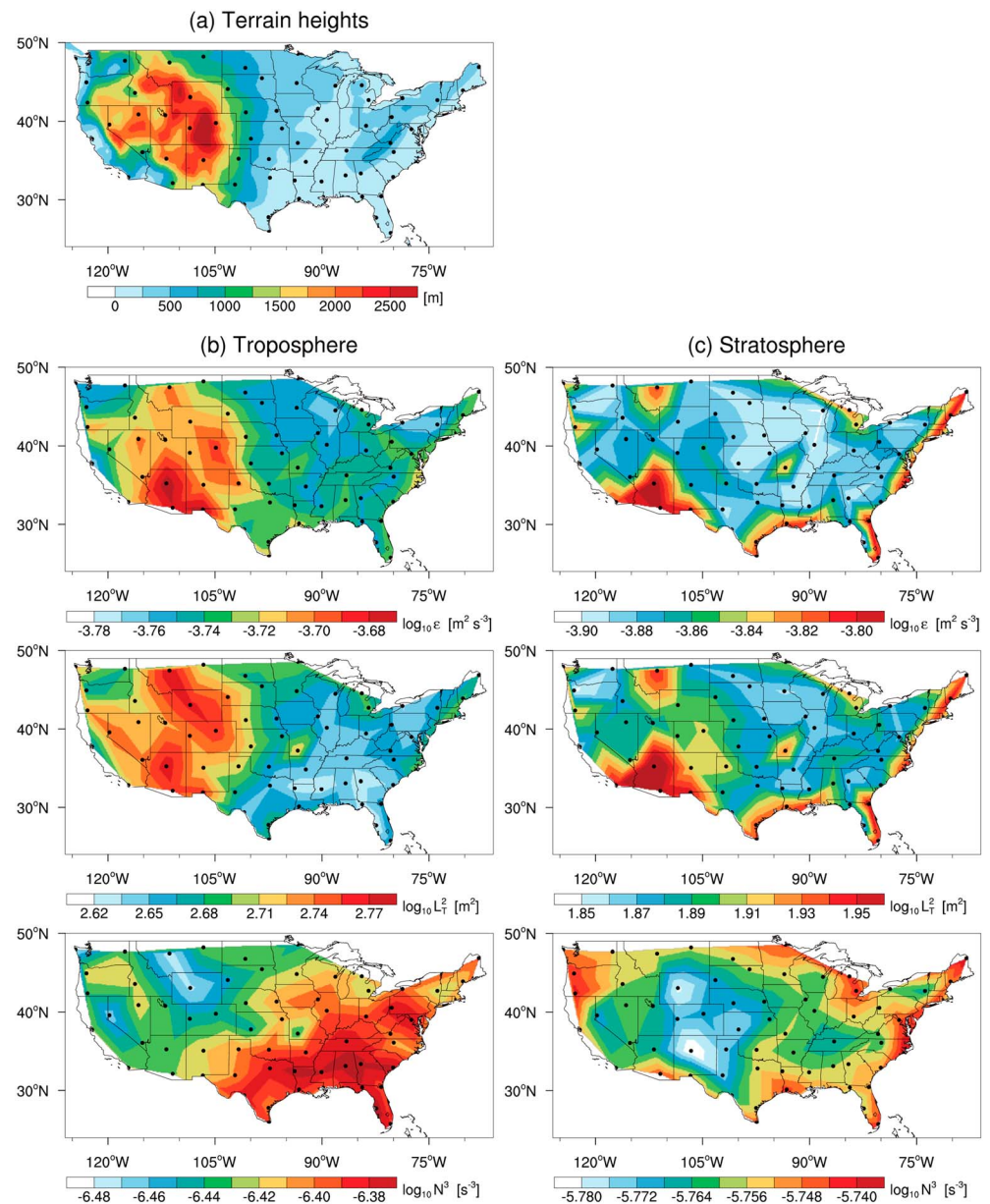
Considering the horizontal distribution of  $L_T$  in the troposphere (Figure 9b, middle), we can see that the horizontal distribution of  $L_T$  is similar to the horizontal distribution of  $\epsilon$ . The horizontal distribution of  $N$  in the troposphere (Figure 9b, lower) is negatively correlated with the horizontal distribution of  $L_T$ , as described in Figure 7. However, since  $\epsilon$  depends on both  $L_T$  and  $N$ ,  $\epsilon$  is partially canceled by the small  $N$  in the northwestern region, where the largest  $L_T$  appeared, and consequently,  $\epsilon$  is smaller than in the other regions. The largest  $L_T$  appears at the Great Falls station (station index 5) in northwestern Montana, but  $N$  is the lowest there, and when  $L_T$  and  $N$  are considered together, the largest  $\epsilon$  appears at the Flagstaff station rather than at the Great Falls station.

Figure 9c shows the horizontal distribution of  $\epsilon$ ,  $L_T$ , and  $N$  in the stratosphere. Note that the scale of each plot is different from that in the troposphere (Figure 9b). In the troposphere, large  $\epsilon$  occurs in the western mountain region, but in the stratosphere, large  $\epsilon$  appear along the southeastern edge of the U.S. mainland; however, relatively large  $\epsilon$  at the Flagstaff and Great Falls stations are also revealed in the stratosphere. The horizontal distribution of  $L_T$  in the stratosphere is consistent with the horizontal distribution of  $\epsilon$  as in the troposphere. However, the horizontal distribution of  $N$  in the stratosphere does not show a clear correlation with the horizontal distribution of  $L_T$ . Instead,  $L_T$  is also large in the large  $N$  region, especially along the East Coast.

The possible sources of large  $\epsilon$  in the mountainous region in the troposphere may be mountain wave breaking and the overturning by orographic convection. Large-amplitude mountain waves may be broken in the troposphere, and orographic convection occurs dominantly in the troposphere. In the stratosphere, large  $\epsilon$  occurs along the southeastern coastline, where a relatively large temperature gradient across the coastline may generate gravity waves that eventually lead to turbulence by breaking. This hypothesis can be supported from a previous study by Wang and Geller (2003) that showed gravity wave energy density calculated using radiosonde data in the U.S. mainland for 4 years (1998–2001) being maximum in the mountainous region in the troposphere and in the southeastern coastline in the stratosphere.

Figure 10 shows the horizontal distribution of monthly mean  $\epsilon$  within each 3-km altitude interval over 4 years from September 2012 to August 2016. The monthly mean  $\epsilon$  for each year is shown in Figures S2–S5, but the interannual variation is not large. As seen previously in Figure 7,  $\epsilon$  tends to increase with increasing altitude in the altitude region  $z = 3$ –12 km (Figures 10a–10c) and appears to be large in the western





**Figure 9.** (a) Terrain heights. (b, c) Horizontal distribution of the mean of the logarithmic (upper) eddy dissipation rate ( $\log_{10}\epsilon$ ), (middle) square of the Thorpe scale ( $\log_{10}L_T^2$ ), and (lower) cube of the Brunt-Väisälä frequency ( $\log_{10}N^3$ ) for 4 years (September 2012 to August 2016) in the troposphere (from 3 km above the station height to the tropopause) and stratosphere (from the tropopause to  $z = 33$  km), respectively. Black dots represent the locations of radiosonde stations. Note that only  $N$  within turbulent layers are used in the lower plots.

mountainous region. In the altitude region  $z = 12$ – $33$  km (Figures 10d–10g),  $\epsilon$  tends to decrease and is not similar to the mountainous pattern. Therefore, the strong mountain influence on turbulence seems to be mainly limited to the troposphere. In Figures 10a, 10c, and 10d,  $\epsilon$  is largest in summer (JJA), but in Figure 10b ( $z = 6$ – $9$  km),  $\epsilon$  is largest in spring (MAM). As shown in Figure 11a, turbulence is strongest at the upper troposphere. In winter and spring, the altitude range of  $z = 6$ – $9$  km corresponds to the upper troposphere. Therefore, turbulence in that altitude range seems to be stronger in winter-spring than in summer-winter. However, because the static stability is strongest in winter, turbulence in the altitude range of  $z = 6$ – $9$  km is likely stronger in spring than in winter. In the higher altitude regions (Figures 10e–10g),  $\epsilon$  shows a similar seasonal variation, with largest values in summer, but this variation is not so clear compared to the variations in the lower altitude regions. To the authors' knowledge, these

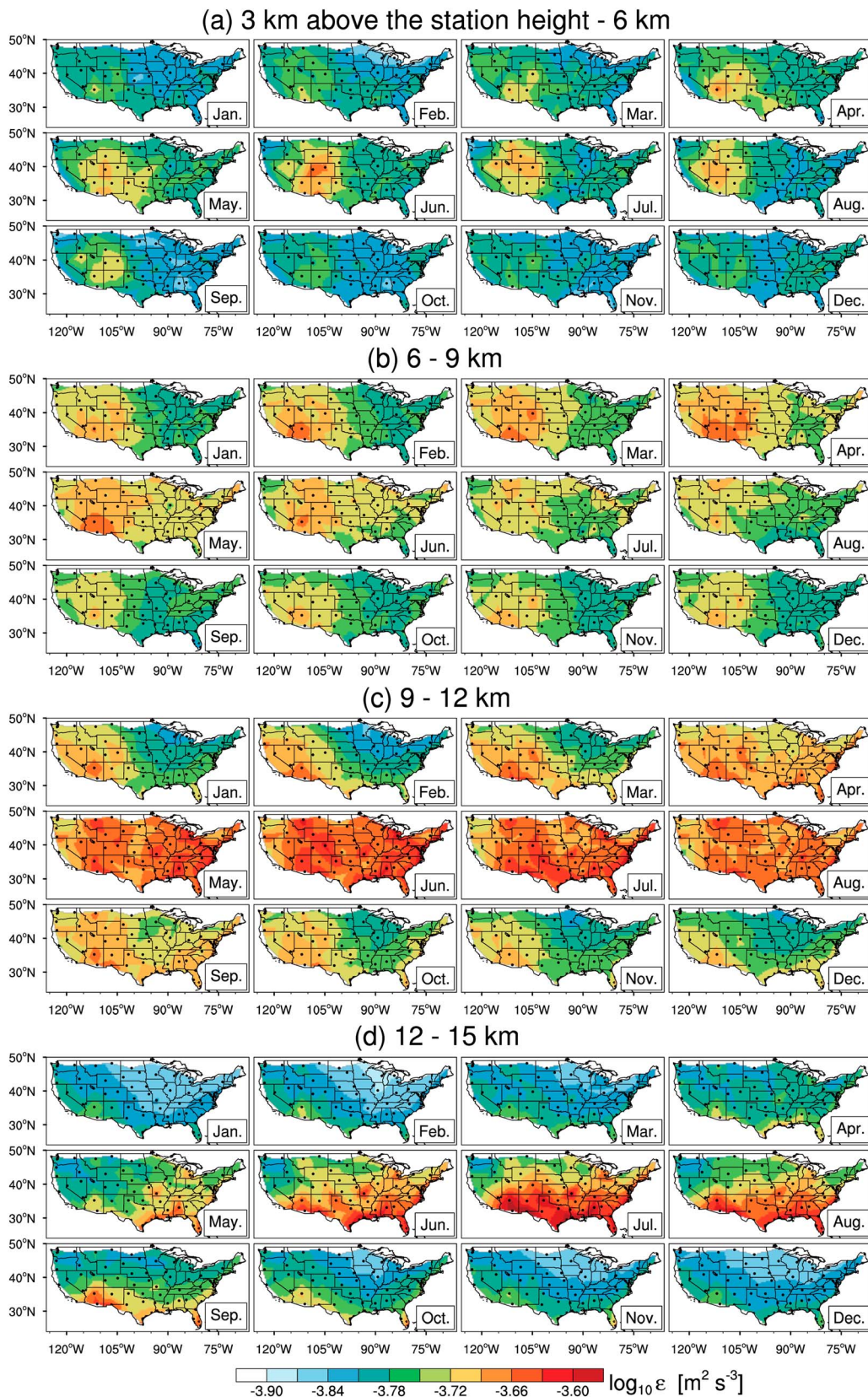


**Figure 10.** Horizontal distribution of the monthly mean of the logarithmic eddy dissipation rate ( $\log_{10}\epsilon$ ) for 4 years (September 2012 to August 2016) within each altitude ranges. Note that, the scale in (e)–(g) is different from that in (a)–(d).



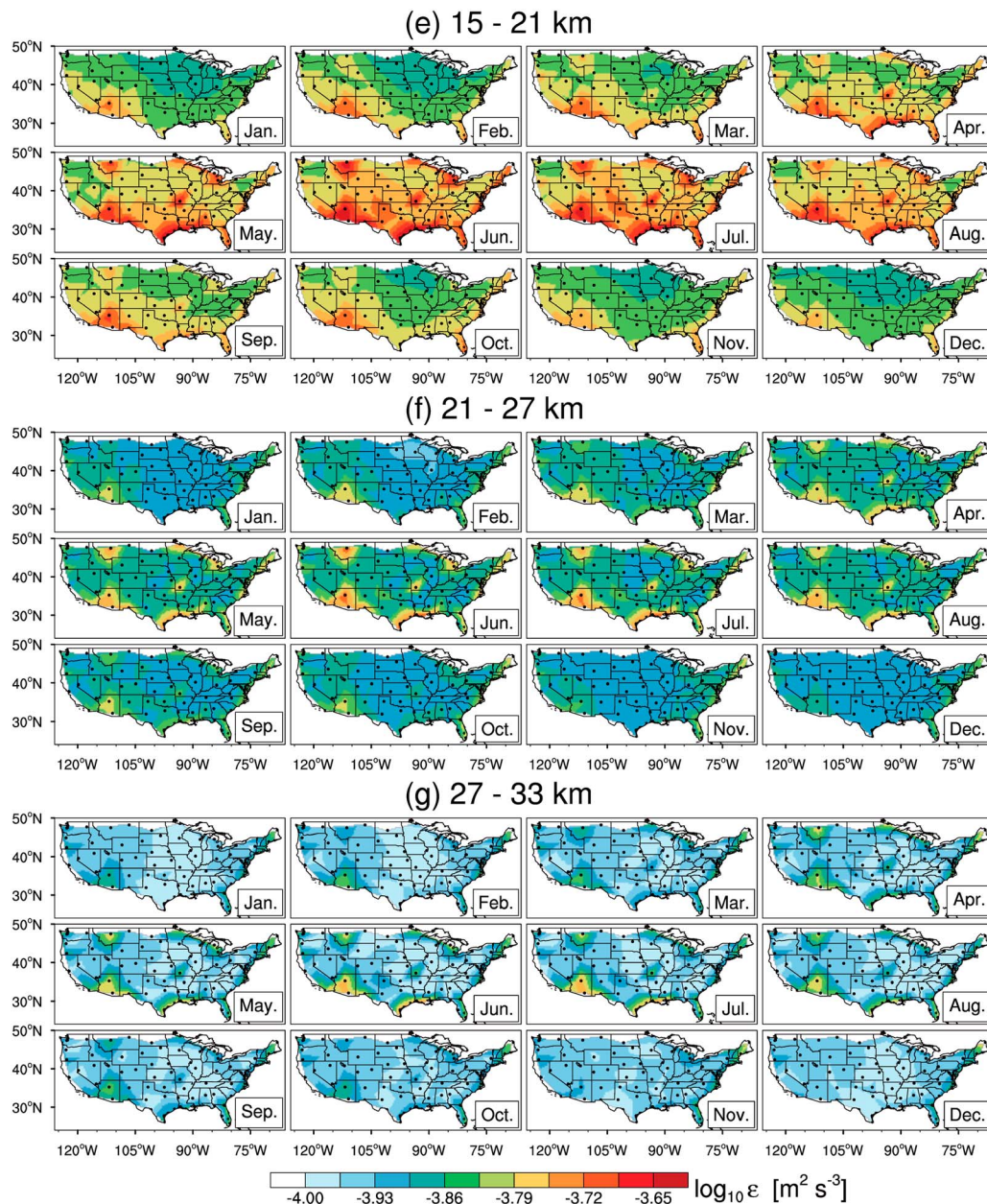
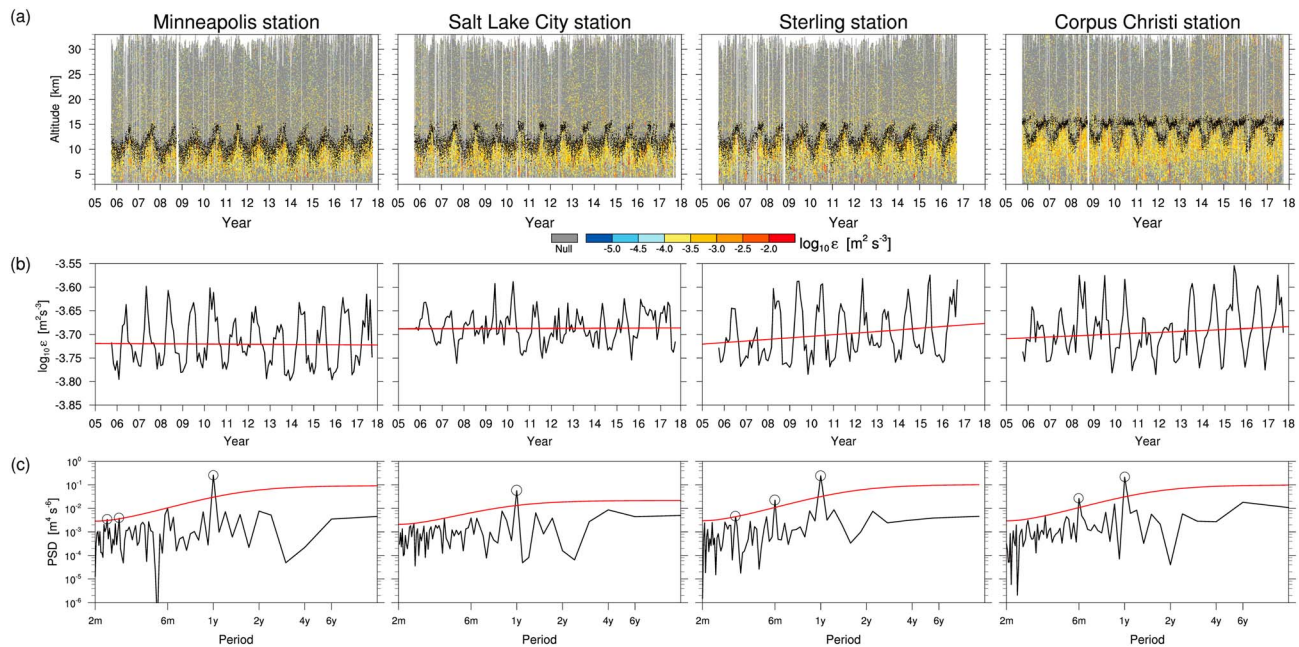


Figure 10. (continued)

horizontal distributions of turbulence and their seasonal variations are first reported in this study. Further study about the sources of turbulence is needed.

### 4.3. Long-Term Variability of Turbulence

The Minneapolis (44.83°N, 93.55°W, station index 10), Salt Lake City (40.77°N, 111.97°W, station index 27), Sterling (38.98°N, 77.47°W, station index 35), and Corpus Christi (27.77°N, 97.50°W, station index 64) stations have been providing HVRRD since October 2005, which can be used to analyze the long-term variability of  $\epsilon$ . Figure 11 shows the long-term variability of  $\epsilon$  calculated from the HVRRD of these four stations. Figure 11a indicates the time-height cross section of  $\log_{10} \epsilon$ , Figure 11b represents the time series of monthly mean  $\log_{10} \epsilon$  from 2 km below the tropopause to the tropopause, and Figure 11c shows the power spectral density (PSD) of the monthly mean  $\log_{10} \epsilon$  in area-preserving form. Note that the area under PSD curve



**Figure 11.** (a) Time-altitude cross section of logarithmic eddy dissipation rate ( $\log_{10}\epsilon$ ), (b) time series of the monthly mean of the  $\log_{10}\epsilon$  from 2 km below the tropopause to the tropopause, and (c) the corresponding power spectral density at four stations: Minneapolis (44.83°N, 93.55°W), Salt Lake City (40.77°N, 111.97°W), Sterling (38.98°N, 77.47°W), and Corpus Christi (27.77°N, 97.50°W). Black dots in (a) indicate the tropopause height. In (a), null (gray) represents the altitude region of no turbulence. The red lines in (b) and (c) indicate a best fit linear trend and the red noise spectrum at the 95% confidence level, respectively. Open circles in (c) show the significant periods with 95% confidence level. The spectrum in (c) is presented in area-preserving form for the log scale of x axis.

corresponds to the total variance, and the unit of the y axis is variance of  $\log_{10}\epsilon$  ( $\text{m}^4/\text{s}^6$ ) when the x axis is the log of the period. To calculate the PSD from the time series data, successive data are needed. However, as shown in Figure 11a, the Minneapolis, Sterling, and Corpus Christi stations have missing data in October 2008. Therefore, we supplemented the monthly mean  $\log_{10}\epsilon$  in October 2008 with the arithmetic means of September and November 2008.

In Figure 11a, a large part of the troposphere is filled with turbulent layers, but the proportion of turbulent layers is relatively small in the stratosphere. Turbulent layers are intermittent and occur at random altitudes, especially in the stratosphere, which supports the assumptions of Dewan's (1981) model. The upper boundary of the turbulent layer in the troposphere coincides well with the tropopause, which is represented by the black dots. This is because turbulence is suppressed due to strong stability in the higher altitude regions above the tropopause (Obukhov, 1971). The turbulent troposphere gradually ascends in spring (MAM), reaches highest altitude in summer (JJA), then gradually descends in autumn (SON), and appears at lowest altitudes in winter (DJF). This seasonal variation of the turbulent layer heights is consistent with the findings of Clayson and Kantha (2008). In addition, the altitude and thickness of the turbulent layers tend to increase in the inverse sense of the station latitude (left to right in Figure 11a). This is likely due to that relatively small  $N$  in low-latitude region results in deeper overturning.

The time series of the monthly mean  $\log_{10}\epsilon$  in Figure 11b shows that  $\epsilon$  has an annual cycle with maximum in summer and minimum in winter. The best fit linear trend line is represented by the red line in each plot. The Minneapolis and Salt Lake City stations show few changes in the long-term trends of  $\log_{10}\epsilon$ , but the Sterling and Corpus Christi stations reveal increasing trends of  $\log_{10}\epsilon$ . The  $t$  statistics for this increasing slope are 2.25 and 2.07 for the Sterling and Corpus Christi stations, respectively, and these values are significant at the 95% confidence level.

The PSD for the time series of the monthly mean  $\log_{10}\epsilon$  is shown in Figure 11c. The annual cycle appears to be dominant in all four stations. The red line in each plot represents a red noise line at the 95% confidence level. There are also significant cycles, such as 2.88- and 2.4-month cycles at the Minneapolis station, 6- and 3.3-month cycles at the Sterling station, and a 6-month cycle at the Corpus Christi station. The origin of these additional cycles are not clear at this moment and will be investigated in a future research focusing on

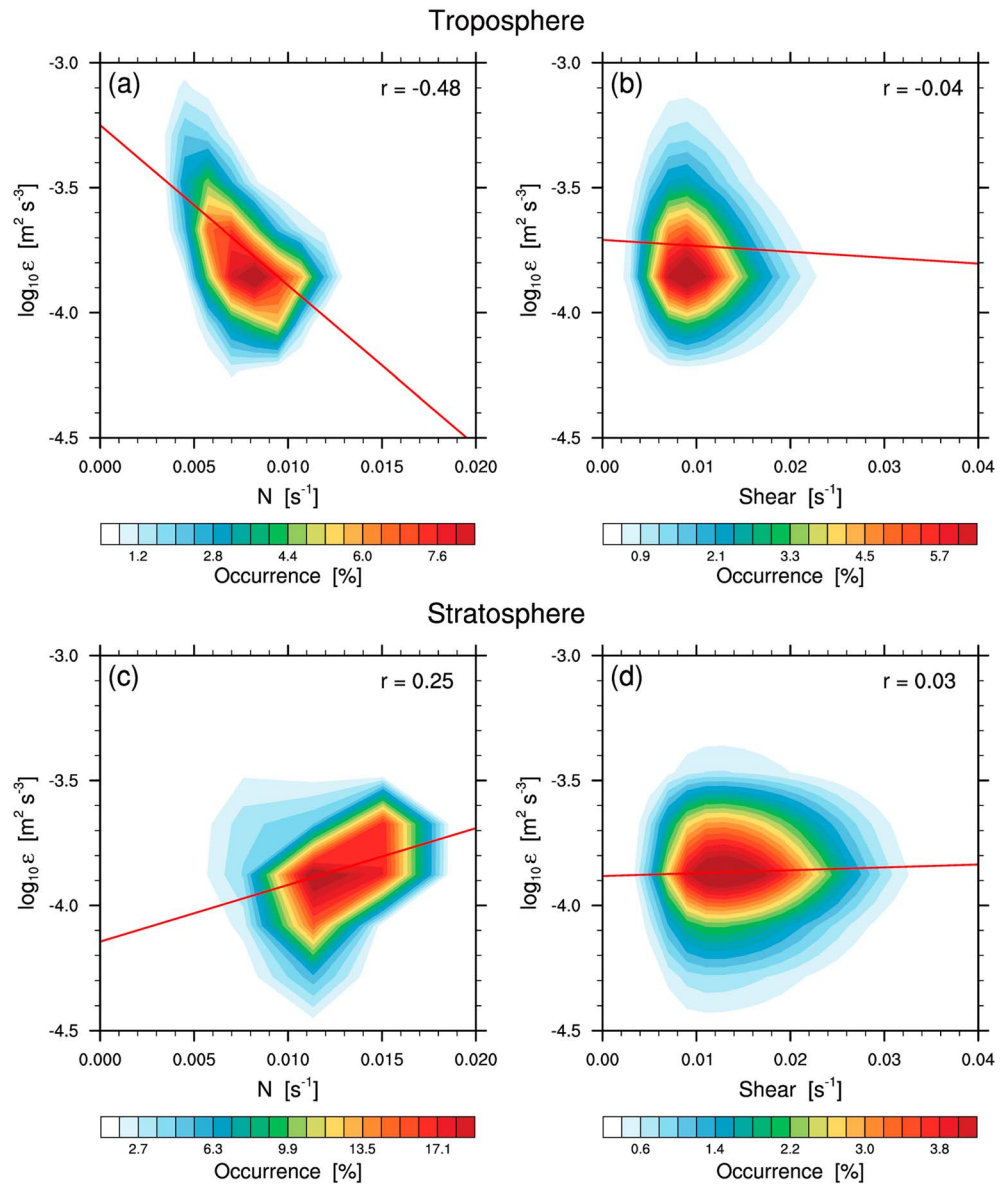


**Figure 12.** Occurrence rate of eddy dissipation rate ( $\log_{10}\epsilon$ ) versus (a, c) Brunt-Väisälä frequency ( $N$ ) and (b, d) vertical wind shear for 4 years (September 2012 to August 2016) in the troposphere (from 3 km above the station height to the tropopause) and stratosphere (from the tropopause to  $z = 33$  km), respectively. The red line in each plot indicates a best fit linear correlation between the two quantities, and the corresponding correlation coefficient  $r$  is indicated in the upper right corner in each plot.

potential sources of the observed turbulence. At the Salt Lake City station in the mountainous region, only the 1-year cycle is significant. The Sterling and Corpus Christi stations, which are located near the sea, have a common 6-month cycle. Although the 6-month cycle does not exceed the 95% confidence level, this cycle is also strong at the Minneapolis station. All four stations do not show any significant cycles longer than a 1-year cycle.

## 5. Discussion

### 5.1. The Distinction Between Convectively Induced Turbulence and Shear-Induced Turbulence

Thorpe analysis estimates the turbulence from the vertical displacement of air parcels calculated by re-sorting observed potential temperature profile; however, the source of the displacement cannot be



distinguished in this method. Therefore, CIT and SIT cannot be distinguished from one another. It is worth noting that radar can in principle distinguish CIT and SIT through analyzing the anisotropy (e.g., Hocking & Hamza, 1997). Here CIT refers to both the turbulence associated with moist convection (i.e., in cloud) and convective overturning ( $N^2 < 0$ ). The Thorpe analysis detects turbulent layers where  $N^2 < 0$ , including moist saturated layers as described in section 3. In this study, only the data above 3 km from the station height are used in order to eliminate the influence in the analysis of air parcels displaced by direct heating near the surface, but the CIT and SIT in the free atmosphere still cannot be distinguished. Bellenger et al. (2015, 2017) estimated the turbulence only outside of the moist saturated layer determined by the method of Zhang et al. (2010) and analyzed it as SIT. Following these authors, we also calculated the turbulent layers for only the altitude regions outside moist saturated layers: However, results are very similar to those including all turbulent layers (not shown), likely because the number of turbulent layers under moist saturated conditions accounts for only 12% of the total number of turbulent layers. It is possible to calculate turbulence for only the altitude regions outside the moist saturated layers and analyze the turbulence value as SIT. However, in addition to convection, moist saturation can also be generated by various mechanisms, such as radiative cooling, cold advection, or water vapor flux. Conversely, even if there is convection, moist saturation does not necessarily occur. Therefore, there is some uncertainty in interpreting the turbulence outside the moist saturated layer as SIT. In the estimation of turbulence using Thorpe analysis, more studies are needed on the criteria for more rigorously judging convection and on the difference in the results of CIT and SIT.

## 5.2. Proportionality Coefficient Between Thorpe Scale $L_T$ and Ozmidov Scale $L_O$

One of the important assumptions in estimating  $\epsilon$  through the Thorpe analysis is that the Thorpe scale  $L_T$  and the Ozmidov scale  $L_O$  have a linear relationship.  $C_K$ , which is the square of the proportional coefficient  $c$  between these two variables, is the most uncertain parameter in the Thorpe analysis. Clayson and Kantha (2008) used  $C_K = 0.3$ , and this value is also used in several other studies (Alappattu & Kunhikrishnan, 2010; Muhsin et al., 2016; Nath et al., 2010; Sunilkumar et al., 2015). Since  $L_O$  cannot be computed from HVRD,  $C_K$  can only be inferred through a reasonable comparison with other observations. Kantha and Hocking (2011) presented  $C_K = 1.0$  through a histogram comparison of  $\epsilon$  calculated from HVRD and from the Harrow very high frequency radar observations. Li et al. (2016) calculated  $\epsilon$  from HVRD and from Middle Atmosphere Alomar Radar System very high frequency radar observations and performed a one-to-one comparison, but the linear regression coefficient was 0.13. As a result, they conducted histogram comparisons of  $\epsilon$  with HVRD and radar, similar to Kantha and Hocking (2011) and presented  $C_K = 1.0$ . As noted in Bellenger et al. (2017), considering that  $\epsilon$  is linearly dependent on  $C_K$ , the difference between  $C_K = 0.3$  and 1.0 changes  $\epsilon$  by a factor of 3. On the other hand, several studies have shown that the value of  $C_K$  appears over a wide range (Balsley et al., 2018; Fritts et al., 2016; Schneider et al., 2015). Schneider et al. (2015) estimated  $L_T$  and  $L_O$  on the same balloon from radiosonde and LITOS, respectively. From this estimation,  $C_K$  was found to be widely distributed over 2 orders of magnitude. Fritts et al. (2016) performed DNS to calculate  $L_T$  and  $L_O$ , indicating that  $C_K$  varies depending on the turbulence type and stage. They suggested that  $C_K = 0.64 - 1.0$  ( $c = 0.8 - 1.0$ ) through suitable averaging. Although a statistical distribution or a specific value was not given, Balsley et al. (2018) also showed that  $C_K$  has a very large variability through the vertical profile of  $c^{-1}$  calculated for each altitude grid. Although these studies used a few profiles over a limited area and period, these are invaluable studies that provide information about  $C_K$  that has rarely been obtained in the atmosphere. Further study of  $C_K$  as a universal value or as a dependent variable is required.

Recently, Scotti (2015) examined the validity of the linear relationship between  $L_O$  and  $L_T$  in the Thorpe analysis, based on idealized turbulent numerical simulations for convective-driven mixing and shear-driven mixing. Scotti (2015) showed that  $L_T/L_O$  for shear-driven turbulence is on the order of 1, while that for convective-driven turbulence is larger than the order of 1. Based on this result, Scotti (2015) suggested an alternative way to estimate  $\epsilon$  based on an energy argument. A practical difficulty in applying this to Thorpe analysis of radiosonde data is the difficulty in determining the nature of the instability that spawned the observed unstable layer. This is discussed further in section 6.

## 5.3. Relationship Between Turbulence and Instability

Turbulence is known to be generated by a variety of mechanisms, such as convective/static instability, dynamic instability, KHI, and gravity wave breaking. To investigate the generation mechanisms of



turbulence, theoretical, observational, and simulation studies have been performed (Fritts et al., 2016; Guarino et al., 2018; Kantha, 2003; Kim & Chun, 2012; Lee & Chun, 2018; Li et al., 2016; Luce et al., 2010; Luce et al., 2010; Moeng & Sullivan, 1994; Osborn, 1980; Sharman et al., 2012; Wolff & Sharman, 2008). In this study, we investigate the occurrence of turbulence in relation to static instability and VWS that can induce dynamic instability, using statistical methods. Figure 12 shows the occurrence rate of  $\epsilon$  with  $N$  and  $\epsilon$  with VWS in the troposphere and stratosphere over 4 years from September 2012 to August 2016.  $N$  and VWS, corresponding to  $\epsilon$  are averaged within each turbulent layer, and  $N$  is calculated from the sorted profile. The linear regression coefficients between  $N$  and  $\epsilon$  are  $-0.48$  and  $0.25$  in the troposphere and stratosphere, respectively. The linear regression coefficients of VWS and  $\epsilon$  are  $-0.04$  and  $0.03$  in the troposphere and stratosphere, respectively. All the regression coefficients are statistically significant with the  $t$  test in 99% confidence level. Although the regression coefficients are very small in Figures 12b and 12d, they appear to be significant due to the very large sample size. In the troposphere, the smaller  $N$ , the larger  $\epsilon$  (Figure 12a). As mentioned in Figures 6 and 9, this relationship can be understood as follows: The lower the stability, the larger the  $L_T$ , and the larger  $L_T$  results in a large  $\epsilon$  due to the relatively narrow distribution of  $N$  (Figure 6). However, in the stratosphere, as  $N$  increases,  $\epsilon$  tends to increase (Figure 12c). This is because the range of  $L_T$  is relatively narrow in the stratosphere (see Figure 6), and as  $N$  becomes larger,  $\epsilon$  becomes larger based on equation (4). Thus, a relatively large VWS in the stratosphere is expected to generate turbulence (Figure 12d). Therefore, we expect a positive correlation between VWS and  $\epsilon$ , similar to Li et al., 2016, Figures 15–17, but such a positive correlation is not observed (Figures 12b and 12d). As previously introduced, the Thorpe analysis is a method of calculating  $\epsilon$ , assuming that the negative potential temperature gradient region is caused by vertical overturning. In other words, all  $\epsilon$  values from the Thorpe analysis appeared in the region where the local  $N^2$  is less than 0. In addition, the correlation between  $\epsilon$  and VWS may be small because mixing already occurs in the turbulent layer. Therefore,  $\epsilon$  in this study does not seem to show a strong positive correlation with VWS.

## 6. Summary and Conclusions

In this study, we estimated Thorpe scale  $L_T$  and TKE dissipation rate  $\epsilon$  in the free atmosphere using the Thorpe analysis and HVRD provided by 68 operational radiosonde stations in the U.S. mainland and analyzed the characteristics of vertical, statistical, and horizontal distributions and long-term variability. The Thorpe analysis is a method of estimating the local turbulence by comparing observed and re-sorted potential temperature profiles. In this study, we followed methods used in previous studies, but there are two points that distinguish our results from those in previous studies. (i) We used a relatively long period of 4-year operational radiosonde data covering the entire U.S. mainland and examined the horizontal distribution of the turbulence. (ii) The long-term turbulence variability is examined from four stations that archived more than 10-year data. The two data periods used in this study are 4 years from September 2012 to August 2016, during which data were provided from 68 stations in the U.S. mainland, and 12 years from October 2005 to September 2017, during which data were provided from four stations (the Sterling station has 11 years of data from October 2005 to September 2016). The main results of this study are as follows.

First, we analyzed the distributions of turbulent layer thickness ( $h$ ),  $\epsilon$ , and  $L_T$  for both the troposphere and stratosphere. The mean values of  $h$  are 159 and 23 m in the troposphere and stratosphere, respectively. The occurrence of  $h$  monotonically decreases with increasing  $h$ . The range of  $\epsilon$  in the troposphere is larger than in the stratosphere, and the mean values are  $1.84 \times 10^{-4}$  and  $1.37 \times 10^{-4} \text{ m}^2/\text{s}^3$  in the troposphere and stratosphere, respectively. The range of  $L_T$  is much wider in the troposphere than in the stratosphere, and the mean values are 28 and 10 m in the troposphere and stratosphere, respectively.

The 4-year vertical turbulence structure showed that the turbulence is stronger in the troposphere than in the stratosphere, and strong turbulence occurred mainly in the low-stability altitude region.  $\epsilon$  is largest at the top of the troposphere in all seasons, especially in summer.  $L_T$  and  $N$  are negatively correlated in both time and altitude. However, since the vertical structure of  $\epsilon$  generally follows that of  $L_T$ ,  $L_T$  seems to have a greater influence than  $N$  on determining the vertical structure of  $\epsilon$ . The interannual variation of the vertical structure of  $\epsilon$  is relatively small compared to the seasonal variation of  $\epsilon$  for the stations examined.

With regard to the horizontal distribution of the turbulence in the U.S. mainland,  $\epsilon$  in the troposphere is large in mountainous regions; therefore, strong turbulence in the troposphere is likely to be associated with mountainous structures. On the other hand, in the stratosphere, large  $\epsilon$  appeared mainly along the coastal

region rather than in mountainous region. In addition, since the horizontal pattern of  $\varepsilon$  corresponds well to the horizontal pattern of  $L_T$ , the influence of  $L_T$  is more dominant than the influence of  $N$  in determining the  $\varepsilon$  in the Thorpe analysis. This is likely the consequence of the relatively narrow distribution of the  $N$  values.

The monthly horizontal distribution of  $\varepsilon$  is examined at altitude intervals of 3 km.  $\varepsilon$  is strongest in summer in the altitude range of  $z = 3\text{--}15$  km, except for  $z = 6\text{--}9$  km. In the altitude range of  $z = 6\text{--}9$  km,  $\varepsilon$  is strongest in spring. Regionally,  $\varepsilon$  is clearly strong in mountainous regions. Vertically,  $\varepsilon$  is strongest in the altitude region  $z = 9\text{--}12$  km. This is consistent with the altitude range at which the highest value was found in the vertical structure of the seasonal mean  $\varepsilon$  (Figure 7). As altitude increases,  $\varepsilon$  gradually decreases in the altitude range  $z = 15\text{--}30$  km. Unlike the situation in the troposphere, there is no clear seasonal variation of  $\varepsilon$  in the stratosphere. The horizontal patterns of  $\varepsilon$  in the altitude range of  $z = 3\text{--}12$  km and of  $z = 12\text{--}33$  km are not similar. The clear correspondence to mountainous structures are not seen in the altitude range of  $z = 12\text{--}33$  km.

In addition, we analyzed the long-term variability of the turbulence using more than 10 years of observational data from four stations. The time-altitude cross section of  $\varepsilon$  shows that turbulent layers continuously appeared in the upper troposphere, and the upper boundary of these turbulent layers coincided well with the tropopause. The altitude of these turbulent layers shows a seasonal variation with high altitudes in summer and low altitudes in winter. We also calculated the monthly mean  $\varepsilon$  from 2 km below the tropopause to the tropopause and found a significant temporal increase in  $\varepsilon$  between 2005 and 2016 (2017) at the Sterling and Corpus Christi stations. In addition, PSD is calculated for the time series of monthly mean  $\varepsilon$ . A 1-year cycle is found to be dominant at all four stations, with a 6-month cycle also significant at both stations near the sea. There is no significant cycle of period longer than 1 year at any of the four stations.

This study used HVRRD from 68 operational radiosonde stations on the U.S. mainland. To improve the predictability of numerical weather forecasting, the number of operational stations that provide HVRRD with more than 1-s resolution is expected to increase (Ingleby et al., 2016). Accordingly, estimating turbulence in a wider horizontal range will be possible in the near future. These results will aid in understanding the global turbulence characteristics that have not yet been obtained due to high costs and observational limits. These results can also be used as additional turbulence data in aviation turbulence studies (Chun et al., 2017), which can ultimately contribute to providing safe and economical aviation services. In addition to turbulence studies, HVRRD can be invaluable data sources in studies of gravity waves, planetary boundary layers, tropopause structures, and numerical forecasting models (Geller et al., 2017).

There are some limitations in Thorpe analysis using HVRRD. First, there may be too thin turbulent layers, and these turbulent layers cannot be detected even with a 5-m vertical resolution of HVRRD (Schneider et al., 2015). Second, it is not straightforward to distinguish the potential sources of the observed turbulence, such as KHI, breaking of various types of gravity waves, and clouds, given that the Thorpe method estimates turbulence only in a negative gradient of potential temperature. Although  $N$  is calculated in the turbulence layer using the re-sorted potential temperature, both  $N$  and VWS inevitably include turbulence effects because of mixing. Therefore,  $Ri$  in the turbulence layer cannot represent the background condition where turbulence may be generated. A feasible way to represent background condition in the turbulence layer, especially, by handling the VWS should be found to investigate sources of the observed turbulence precisely, which remains for future research.

## Appendix A

**Table A1**

*Information of the Operational Radiosonde Stations Providing High Vertical-Resolution Radiosonde Data in the United States*

Station index	WMO ID	Station name	Latitude	Longitude
1	72747	International Falls	48.57	−93.38
2	72768	Glasgow	48.20	−106.62
3	72797	Quillayute	47.95	−124.55
4	72786	Spokane	47.68	−117.63

**Table A1** (continued)

Station index	WMO ID	Station name	Latitude	Longitude
5	72776	Great Falls	47.45	−111.38
6	72712	Caribou	46.87	−68.02
7	72764	Bismarck	46.77	−100.75
8	72659	Aberdeen	45.45	−98.42
9	72694	Salem	44.92	−123.02
10	72649	Minneapolis	44.83	−93.55
11	72634	Gaylord	44.55	−84.43
12	72645	Green bay	44.48	−88.13
13	72662	Rapid city	44.07	−103.21
14	74389	Gray	43.89	−70.25
15	72681	Boise	43.57	−116.22
16	72672	Riverton	43.06	−108.47
17	72528	Buffalo	42.93	−78.73
18	72632	Detroit	42.70	−83.47
19	72518	Albany	42.45	−73.49
20	72597	Medford	42.37	−122.87
21	74494	Chatham	41.67	−69.97
22	74455	Davenport	41.60	−90.57
23	72558	Valley	41.32	−96.37
24	72562	North Platte	41.13	−100.68
25	72582	Elko	40.87	−115.73
26	72501	New York City	40.87	−72.87
27	72572	Salt Lake City	40.77	−111.97
28	72520	Pittsburgh	40.53	−80.23
29	74560	Lincoln	40.15	−89.33
30	72469	Denver	39.77	−104.88
31	72489	Reno	39.57	−119.80
32	72426	Wilmington	39.42	−83.82
33	72476	Grand Junction	39.12	−108.53
34	72456	Topeka	39.07	−95.62
35	72403	Sterling	38.98	−77.47
36	72451	Dodge City	37.77	−99.97
37	72493	Oakland	37.75	−122.22
38	72440	Springfield	37.23	−93.40
39	72318	Roanoke	37.20	−80.41
40	72327	Nashville	36.25	−86.57
41	72317	Greensboro	36.08	−79.95
42	72388	Las Vegas	36.05	−115.18
43	72363	Amarillo	35.23	−101.70
44	72376	Flagstaff	35.23	−111.82
45	72357	Norman	35.18	−97.44
46	72365	Albuquerque	35.05	−106.62
47	72340	Little Rock	34.83	−92.27
48	72305	Morehead City	34.70	−76.80
49	72215	Peachtree City	33.35	−84.56
50	72230	Birmingham	33.10	−86.70
51	72208	Charleston	32.90	−80.03
52	72293	San Diego	32.87	−117.15
53	72249	Fort Worth	32.80	−97.30
54	72248	Shreveport	32.45	−93.83
55	72235	Jackson	32.32	−90.07

Table A1 (continued)

Station index	WMO ID	Station name	Latitude	Longitude
56	72274	Tuscon	32.12	−110.93
57	72265	Midland	31.93	−102.20
58	72364	Santa Teresa	31.90	−106.70
59	72206	Jacksonville	30.43	−81.70
60	72214	Tallahassee	30.38	−84.37
61	72233	Slidell	30.33	−89.82
62	72240	Lake Charles	30.12	−93.22
63	72261	Del Rio	29.37	−100.92
64	72251	Corpus Christi	27.77	−97.50
65	72210	Tampa Bay	27.70	−82.40
66	72250	Brownsville	25.90	−97.43
67	72202	Miami	25.75	−80.38
68	72201	Key West	24.50	−81.80

Note. WMO = World Meteorological Organization.

## Acknowledgments

The authors thank three anonymous reviewers for many helpful comments and suggestions. This research was supported by the Korea Meteorological Administration Research and Development Program under Grant KMIPA KMI2018-07810. The radiosonde data were downloaded from the Stratosphere-troposphere Processes And their Role in Climate (SPARC) Data Centre at Stony Brook University, NY, USA (available online at <http://www.sparc-climate.org/data-center/data-access/us-radiosonde>) and the National Oceanic and Atmospheric Administration (NOAA) at 1401 Constitution Avenue NW, Washington, DC, USA (available online at <ftp://ftp.ncdc.noaa.gov/pub/data/ua/rrs-data/>). We also acknowledge using software that was generously given to us by Dr. Peter Love of the University of Tasmania.

## References

- Alappattu, D. P., & Kunhikrishnan, P. K. (2010). First observations of turbulence parameters in the troposphere over the Bay of Bengal and the Arabian Sea using radiosonde. *Journal of Geophysical Research*, 115, D06105. <https://doi.org/10.1029/2009JD012916>
- Allen, S. J., & Vincent, R. A. (1995). Gravity wave activity in the lower atmosphere: Seasonal and latitudinal variations. *Journal of Geophysical Research*, 100(D1), 1327–1350. <https://doi.org/10.1029/94JD02688>
- Balsley, B. B., Kantha, L., & Colgan, W. (2010). On the use of slow ascent meter-scale sampling (SAMS) radiosondes for observing overturning events in the free atmosphere. *Journal of Atmospheric and Oceanic Technology*, 27(4), 766–775. <https://doi.org/10.1175/2009JTECHA1310.1>
- Balsley, B. B., Lawrence, D. A., Fritts, D. C., Wang, L., Wan, K., & Werne, J. (2018). Fine structure, instabilities, and turbulence in the lower atmosphere: High-resolution in Situ Slant-Path measurements with the DataHawk UAV and comparisons with numerical modeling. *Journal of Atmospheric and Oceanic Technology*, 35(3), 619–642. <https://doi.org/10.1175/JTECH-D-16-0037.1>
- Bellenger, H., Katsumata, M., & Yoneyama, K. (2015). Turbulent mixing and its impact on lower tropospheric moisture over tropical ocean. *Geophysical Research Letters*, 42, 3030–3037. <https://doi.org/10.1002/2015GL063868>
- Bellenger, H., Wilson, R., Davison, J. L., Duvel, J. P., Xu, W., Lott, F., & Katsumata, M. (2017). Tropospheric turbulence over the tropical open ocean: Role of gravity waves. *Journal of the Atmospheric Sciences*, 74(4), 1249–1271. <https://doi.org/10.1175/JAS-D-16-0135.1>
- Bertin, F., Barat, J., & Wilson, R. (1997). Energy dissipation rates, eddy diffusivity, and the Prandtl number: An in situ experimental approach and its consequences on radar estimate of turbulent parameters. *Radio Science*, 32(2), 791–804. <https://doi.org/10.1029/96RS03691>
- Birner, T. (2006). Fine-scale structure of the extratropical tropopause region. *Journal of Geophysical Research*, 111, D04104. <https://doi.org/10.1029/2005JD006301>
- Birner, T., Dörnbrack, A., & Schumann, U. (2002). How sharp is the tropopause at midlatitudes? *Geophysical Research Letters*, 29(14), 1700. <https://doi.org/10.1029/2002GL015142>
- Cho, J. Y., & Lindborg, E. (2001). Horizontal velocity structure functions in the upper troposphere and lower stratosphere: 1. Observations. *Journal of Geophysical Research*, 106, 10,223–10,232. <https://doi.org/10.1029/2000JD900814>
- Cho, J. Y. N., Newell, R. E., Anderson, B. E., Barrick, J. D. W., & Thornhill, K. L. (2003). Characterizations of tropospheric turbulence and stability layers from aircraft observations. *Journal of Geophysical Research*, 108(D20), 8784. <https://doi.org/10.1029/2002JD002820>
- Chun, H.-Y., Goh, J.-S., & Kim, Y.-H. (2007). Characteristics of inertio-gravity waves revealed in rawinsonde data observed in Korea during 20 August to 5 September 2002. *Journal of Geophysical Research*, 112, D16108. <https://doi.org/10.1029/2006JD008348>
- Chun, H.-Y., Kim, J.-H., Lee, D.-B., Kim, S.-H., Strahan, M., Pettegrew, B., et al. (2017). Research collaborations for better predictions of aviation weather hazards. *Bulletin of the American Meteorological Society*, 98(5), ES103–ES107. <https://doi.org/10.1175/BAMS-D-17-0010.1>
- Chun, H.-Y., Song, I.-S., & Baik, J.-J. (2006). Seasonal variations of gravity waves revealed in rawinsonde data at Pohang, Korea. *Meteorology and Atmospheric Physics*, 93(3–4), 255–273. <https://doi.org/10.1007/s00703-005-0164-5>
- Clayson, C. A., & Kantha, L. (2008). On turbulence and mixing in the free atmosphere inferred from high-resolution soundings. *Journal of Atmospheric and Oceanic Technology*, 25(6), 833–852. <https://doi.org/10.1175/2007JTECHA992.1>
- Cohn, S. A. (1995). Radar measurements of turbulent eddy dissipation rate in the troposphere: A comparison of techniques. *Journal of Atmospheric and Oceanic Technology*, 12(1), 85–95. [https://doi.org/10.1175/1520-0426\(1995\)012<0085:RMOTED>2.0.CO;2](https://doi.org/10.1175/1520-0426(1995)012<0085:RMOTED>2.0.CO;2)
- Dee, D. P., Uppala, S. M., Simmons, A. J., Berrisford, P., Poli, P., Kobayashi, S., et al. (2011). The ERA-Interim reanalysis: Configuration and performance of the data assimilation system. *Quarterly Journal of the Royal Meteorological Society*, 137(656), 553–597. <https://doi.org/10.1002/qj.828>
- Dehghan, A., & Hocking, W. K. (2011). Instrumental errors in spectral-width turbulence measurements by radars. *Journal of Atmospheric and Solar-Terrestrial Physics*, 73(9), 1052–1068. <https://doi.org/10.1016/j.jastp.2010.11.011>
- Dehghan, A., Hocking, W. K., & Srinivasan, R. (2014). Comparisons between multiple in-situ aircraft turbulence measurements and radar in the troposphere. *Journal of Atmospheric and Solar-Terrestrial Physics*, 118, 64–77. <https://doi.org/10.1016/j.jastp.2013.10.009>
- Dewan, E. M. (1981). Turbulent vertical transport due to thin intermittent mixing layers in the stratosphere and other stable fluids. *Science*, 211(4486), 1041–1042. <https://doi.org/10.1126/science.211.4486.1041>

- Dillon, T. M. (1982). Vertical overturns: A comparison of Thorpe and Ozmidov length scales. *Journal of Geophysical Research*, 87(C12), 9601–9613. <https://doi.org/10.1029/JC087iC12p09601>
- Durran, D. R., & Klemp, J. B. (1982). On the effects of moisture on the Brunt-Väisälä frequency. *Journal of the Atmospheric Sciences*, 39(10), 2152–2158. [https://doi.org/10.1175/1520-0469\(1982\)039<2152:OTEOMO>2.0.CO;2](https://doi.org/10.1175/1520-0469(1982)039<2152:OTEOMO>2.0.CO;2)
- Durre, I., Yin, X., Vose, R. S., Applequist, S., & Arnfield, J. (2018). Enhancing the data coverage in the Integrated Global Radiosonde Archive. *Journal of Atmospheric and Oceanic Technology*, 35(9), 1753–1770. <https://doi.org/10.1175/JTECH-D-17-0223.1>
- Frehlich, R., & Sharman, R. (2010). Climatology of velocity and temperature turbulence statistics determined from rawinsonde and ACARS/AMDAR data. *Journal of Applied Meteorology and Climatology*, 49(6), 1149–1169. <https://doi.org/10.1175/2010JAMC2196.1>
- Fritts, D. C., Wang, L., Geller, M. A., Lawrence, D. A., Werne, J., & Balsley, B. B. (2016). Numerical modeling of multiscale dynamics at a high Reynolds number: Instabilities, turbulence, and an assessment of Ozmidov and Thorpe scales. *Journal of the Atmospheric Sciences*, 73(2), 555–578. <https://doi.org/10.1175/JAS-D-14-0343.1>
- Geller, M. A., Chun, H.-Y., & Love, P. T. (2016). FISAPS-An emerging SPARC activity. *SPARC*, 47, 8–10.
- Geller, M. A., & Love, P. T. (2013). Research using high vertical-resolution radiosonde data. *SPARC*, 40, 29–32.
- Geller, M. A., Wang, L., Chun, H.-Y., & Love, P. T. (2017). Fine-scale atmospheric processes and structures. *SPARC*, 49, 10–20.
- Grubišić, V., Doyle, J. D., Kuetner, J., Mobbs, S., Smith, R. B., Whiteman, C. D., et al. (2008). The terrain-induced rotor experiment: A field campaign overview including observational highlights. *Bulletin of the American Meteorological Society*, 89(10), 1513–1534. <https://doi.org/10.1175/2008bams2487.1>
- Guarino, M.-V., Teixeira, M. A. C., Keller, T. L., & Sharman, R. D. (2018). Mountain-wave turbulence in the presence of directional wind shear over the Rocky mountains. *Journal of the Atmospheric Sciences*, 75(4), 1285–1305. <https://doi.org/10.1175/JAS-D-17-0128.1>
- Hamilton, K., & Vincent, R. A. (1995). High-resolution radiosonde data offer new prospects for research. *Eos, Transactions American Geophysical Union*, 76(49), 497–506. <https://doi.org/10.1029/95EO00308>
- Hocking, W. K. (1988). Two years of continuous measurements of turbulence parameters in the upper mesosphere and lower thermosphere made with a 2-MHz radar. *Journal of Geophysical Research*, 93(D3), 2475–2491. <https://doi.org/10.1029/JD093iD03p02475>
- Hocking, W. K., & Hamza, A. M. (1997). A quantitative measure of the degree of anisotropy of turbulence in terms of atmospheric parameters, with particular relevance to radar studies. *Journal of Atmospheric and Solar-Terrestrial Physics*, 59(9), 1011–1020. [https://doi.org/10.1016/S1364-6826\(96\)00074-0](https://doi.org/10.1016/S1364-6826(96)00074-0)
- Hocking, W. K., & Mu, P. K. L. (1997). Upper and middle tropospheric kinetic energy dissipation rates from measurements of Cn2—Review of theories, in-situ investigations, and experimental studies using the Buckland Park atmospheric radar in Australia. *Journal of Atmospheric and Solar-Terrestrial Physics*, 59(14), 1779–1803. [https://doi.org/10.1016/S1364-6826\(97\)00020-5](https://doi.org/10.1016/S1364-6826(97)00020-5)
- Hoshino, S., Kobayashi, H., Koike, T., Hashiguchi, H., Kawamura, S., Adachi, A., et al. (2016). Comparison between turbulence eddy dissipation rates retrieved by wind profiler radar and in situ radiosondes. *Papers in Meteorology and Geophysics*, 66, 39–55. <https://doi.org/10.2467/mripapers.66.39>
- ICAO (International Civil Aviation Organization). (2016). Meteorological service for international air navigation. *Annex 3 to the Convention on International Civil Aviation*, 19th Edition, 134 pp.
- Ingleby, B., Pauley, P., Kats, A., Ator, J., Keyser, D., Doerenbecher, A., et al. (2016). Progress toward high-resolution, real-time radiosonde reports. *Bulletin of the American Meteorological Society*, 97(11), 2149–2161. <https://doi.org/10.1175/BAMS-D-15-00169.1>
- Kantha, L., & Hocking, W. (2011). Dissipation rates of turbulence kinetic energy in the free atmosphere: MST radar and radiosondes. *Journal of Atmospheric and Solar-Terrestrial Physics*, 73(9), 1043–1051. <https://doi.org/10.1016/j.jastp.2010.11.024>
- Kantha, L. H. (2003). On an improved model for the turbulent PBL. *Journal of the Atmospheric Sciences*, 60(17), 2239–2246. [https://doi.org/10.1175/1520-0469\(2003\)060<2239:OAIMFT>2.0.CO;2](https://doi.org/10.1175/1520-0469(2003)060<2239:OAIMFT>2.0.CO;2)
- Ki, M.-O., & Chun, H.-Y. (2010). Characteristics and sources of inertia-gravity waves revealed in the KEOP-2007 radiosonde data. *Asia-Pacific Journal of Atmospheric Sciences*, 46(3), 261–277. <https://doi.org/10.1007/s13143-010-1001-4>
- Kim, J.-H., & Chun, H.-Y. (2012). A numerical simulation of convectively induced turbulence above deep convection. *Journal of Applied Meteorology and Climatology*, 51(6), 1180–1200. <https://doi.org/10.1175/JAMC-D-11-0140.1>
- Kohma, M., Sato, K., Tomikawa, Y., Nishimura, K., & Sato, T. (2019). Estimate of turbulent energy dissipation rate from the VHF radar and radiosonde observations in the Antarctic. *Journal of Geophysical Research: Atmospheres*, 124, 2976–2993. <https://doi.org/10.1029/2018JD029521>
- Lalas, D. P., & Einaudi, F. (1974). On the correct use of the wet adiabatic lapse rate in stability criteria of a saturated atmosphere. *Journal of Applied Meteorology*, 13(3), 318–324. [https://doi.org/10.1175/1520-0450\(1974\)013<0318:OTCUOT>2.0.CO;2](https://doi.org/10.1175/1520-0450(1974)013<0318:OTCUOT>2.0.CO;2)
- Lee, D.-B., & Chun, H.-Y. (2018). A numerical study of aviation turbulence encountered on 13 February 2013 over the Yellow Sea between China and the Korean Peninsula. *Journal of Applied Meteorology and Climatology*, 57(4), 1043–1060. <https://doi.org/10.1175/JAMC-D-17-0247.1>
- Li, Q., Rapp, M., Schrön, A., Schneider, A., & Stober, G. (2016). Derivation of turbulent energy dissipation rate with the Middle Atmosphere Alomar Radar System (MAARSY) and radiosondes at Andoya, Norway. *Annales Geophysicae*, 34(12), 1209–1229. <https://doi.org/10.5194/angeo-34-1209-2016>
- Lilly, D. K., Waco, D. E., & Adelfang, S. I. (1974). Stratospheric mixing estimated from high-altitude turbulence measurements. *Journal of Applied Meteorology*, 13(4), 488–493. [https://doi.org/10.1175/1520-0450\(1974\)013<0488:SMEFHA>2.0.CO;2](https://doi.org/10.1175/1520-0450(1974)013<0488:SMEFHA>2.0.CO;2)
- Lindborg, E. (1999). Can the atmospheric kinetic energy spectrum be explained by two-dimensional turbulence? *Journal of Fluid Mechanics*, 388, 259–288. <https://doi.org/10.1017/S0022112099004851>
- Liu, X., Xu, J., & Yuan, W. (2014). Diurnal variations of turbulence parameters over the tropical oceanic upper troposphere during SCSMEX. *Science China Technological Sciences*, 57(2), 351–359. <https://doi.org/10.1007/s11431-013-5445-5>
- Love, P. T., & Geller, M. A. (2012). Research using high (and higher) resolution radiosonde data. *Eos, Transactions American Geophysical Union*, 93(35), 337–338. <https://doi.org/10.1029/2012EO350001>
- Lübken, F.-J. (1992). On the extraction of turbulent parameters from atmospheric density fluctuations. *Journal of Geophysical Research*, 97(D18), 20,385–20,395. <https://doi.org/10.1029/92JD01916>
- Luce, H., Mega, T., Yamamoto, M. K., Yamamoto, M., Hashiguchi, H., Fukao, S., et al. (2010). Observations of Kelvin-Helmholtz instability at a cloud base with the middle and upper atmosphere (MU) and weather radars. *Journal of Geophysical Research*, 115, D19116. <https://doi.org/10.1029/2009JD013519>
- Luce, H., Nakamura, T., Yamamoto, M. K., Yamamoto, M., & Fukao, S. (2010). MU radar and lidar observations of clear-air turbulence underneath cirrus. *Monthly Weather Review*, 138(2), 438–452. <https://doi.org/10.1175/2009mwr2927.1>



- Luce, H., Wilson, R., Dalaudier, F., Hashiguchi, H., Nishi, N., Shibagaki, Y., & Nakajo, T. (2014). Simultaneous observations of tropospheric turbulence from radiosondes using Thorpe analysis and the VHF MU radar. *Radio Science*, 49, 1106–1123. <https://doi.org/10.1002/2013RS005355>
- Moeng, C.-H., & Sullivan, P. P. (1994). A comparison of shear- and buoyancy-driven planetary boundary layer flows. *Journal of the Atmospheric Sciences*, 57(7), 999–1022. [https://doi.org/10.1175/1520-0469\(1994\)051<0999:ACOSAB>2.0.CO;2](https://doi.org/10.1175/1520-0469(1994)051<0999:ACOSAB>2.0.CO;2)
- Muhsin, M., Sunilkumar, S. V., Ratnam, M. V., Parameswaran, K., Murthy, B. V. K., Ramkumar, G., & Rajeev, K. (2016). Diurnal variation of atmospheric stability and turbulence during different seasons in the troposphere and lower stratosphere derived from simultaneous radiosonde observations at two tropical stations, in the Indian Peninsula. *Atmospheric Research*, 180, 12–23. <https://doi.org/10.1016/j.atmosres.2016.04.021>
- Nastrom, G. D., & Eaton, F. D. (1997). Turbulence eddy dissipation rates from radar observations at 5–20 km at White Sands Missile Range, New Mexico. *Journal of Geophysical Research*, 102(D16), 19,495–19,505. <https://doi.org/10.1029/97JD01262>
- Nastrom, G. D., & Eaton, F. D. (2005). Seasonal variability of turbulence parameters at 2 to 21 km from MST radar measurements at Vandenberg Air Force Base, California. *Journal of Geophysical Research*, 110, D19110. <https://doi.org/10.1029/2005JD005782>
- Nath, D., Ratnam, M. V., Patra, A. K., Murthy, B. V. K., & Rao, S. V. B. (2010). Turbulence characteristics over tropical station Gadanki (13.5° N, 79.2° E) estimated using high-resolution GPS radiosonde data. *Journal of Geophysical Research*, 115, D07102. <https://doi.org/10.1029/2009JD012347>
- Obukhov, A. M. (1971). Turbulence in an atmosphere with a non-uniform temperature. *Boundary-layer meteorology*, 2(1), 7–29. <https://doi.org/10.1007/BF00718085>
- Osborn, T. R. (1980). Estimates of the local rate of vertical diffusion from dissipation measurements. *Journal of Physical Oceanography*, 10(1), 83–89. [https://doi.org/10.1175/1520-0485\(1980\)010<0083:EOTLRO>2.0.CO;2](https://doi.org/10.1175/1520-0485(1980)010<0083:EOTLRO>2.0.CO;2)
- Osman, M. K., Hocking, W. K., & Tarasick, D. W. (2016). Parameterization of large-scale turbulent diffusion in the presence of both well-mixed and weakly mixed patchy layers. *Journal of Atmospheric and Solar-Terrestrial Physics*, 143–144, 14–36. <https://doi.org/10.1016/j.jastp.2016.02.025>
- Ozmidov, R. V. (1965). On the turbulent exchange in a stably stratified ocean. *Izv. Acad. Sci. USSR. Atmospheric and Oceanic Physics*, 1, 861–871.
- Sato, K., & Yoshiki, M. (2008). Gravity wave generation around the polar vortex in the stratosphere revealed by 3-hourly radiosonde observations at Syowa Station. *Journal of the Atmospheric Sciences*, 65(12), 3719–3735. <https://doi.org/10.1175/2008JAS2539.1>
- Schneider, A., Gerding, M., & Lübken, F.-J. (2015). Comparing turbulent parameters obtained from LITOS and radiosonde measurements. *Atmospheric Chemistry and Physics*, 15(4), 2159–2166. <https://doi.org/10.5194/acp-15-2159-2015>
- Scotti, A. (2015). Biases in Thorpe-scale estimates of turbulence dissipation. Part II: Energetics arguments and turbulence simulations. *Journal of Physical Oceanography*, 45(10), 2522–2543. <https://doi.org/10.1175/JPO-D-14-0092.1>
- Seidel, D. J., Ao, C. O., & Li, K. (2010). Estimating climatological planetary boundary layer heights from radiosonde observations: Comparison of methods and uncertainty analysis. *Journal of Geophysical Research*, 115, D16113. <https://doi.org/10.1029/2009JD013680>
- Seidel, D. J., & Randel, W. J. (2006). Variability and trends in the global tropopause estimated from radiosonde data. *Journal of Geophysical Research*, 111, D21101. <https://doi.org/10.1029/2006JD007363>
- Sharman, R. D., Cornman, L. B., Meymaris, G., Pearson, J., & Farrar, T. (2014). Description and derived climatologies of automated in situ eddy-dissipation-rate reports of atmospheric turbulence. *Journal of Applied Meteorology and Climatology*, 53(6), 1416–1432. <https://doi.org/10.1175/JAMC-D-13-0329.1>
- Sharman, R. D., Trier, S. B., Lane, T. P., & Doyle, J. D. (2012). Sources and dynamics of turbulence in the upper troposphere and lower stratosphere: A review. *Geophysical Research Letters*, 39, L12803. <https://doi.org/10.1029/2012GL051996>
- Singh, N., Joshi, R. R., Chun, H.-Y., Pant, G. B., Damle, S. H., & Vashishtha, R. D. (2008). Seasonal, annual and inter-annual features of turbulence parameters over the tropical station Pune (18°32'N, 73°51'E) observed with UHF wind profiler. *Annales Geophysicae*, 26(12), 3677–3692. <https://doi.org/10.5194/angeo-26-3677-2008>
- Smalikho, I., Köpp, F., & Rahm, S. (2005). Measurement of atmospheric turbulence by 2-μm Doppler lidar. *Journal of Atmospheric and Oceanic Technology*, 22(11), 1733–1747. <https://doi.org/10.1175/JTECH1815.1>
- Sorbjan, Z., & Balsley, B. B. (2008). Microstructure of turbulence in the stably stratified boundary layer. *Boundary-Layer Meteorology*, 129(2), 191–210. <https://doi.org/10.1007/s10546-008-9310-1>
- Sun, Z., Ning, H., Song, S., & Yan, D. (2016). First observations of elevated ducts associated with intermittent turbulence in the stable boundary layer over Bosten Lake, China. *Journal of Geophysical Research: Atmospheres*, 121, 11,201–11,214. <https://doi.org/10.1002/2016JD024793>
- Sunilkumar, S. V., Muhsin, M., Parameswaran, K., Venkat Ratnam, M., Ramkumar, G., Rajeev, K., et al. (2015). Characteristics of turbulence in the troposphere and lower stratosphere over the Indian Peninsula. *Journal of Atmospheric and Solar-Terrestrial Physics*, 133, 36–53. <https://doi.org/10.1016/j.jastp.2015.07.015>
- Sunilkumar, S. V., Muhsin, M., Ratnam, M. V., Parameswaran, K., Murthy, B. V. K., & Emmanuel, M. (2017). Boundaries of tropical tropopause layer (TTL): A new perspective based on thermal and stability profiles. *Journal of Geophysical Research: Atmospheres*, 122, 741–754. <https://doi.org/10.1002/2016JD025217>
- Thorpe, S. A. (1977). Turbulence and mixing in a Scottish Loch. *Philosophical Transactions of the Royal Society A Mathematical, Physical and Engineering Sciences*, 286(1334), 125–181. <https://doi.org/10.1098/rsta.1977.0112>
- Thorpe, S. A. (2005). *The turbulent ocean*. Cambridge University Press. <https://doi.org/10.1017/CBO9780511819933>
- Vanneste, J., & Haynes, P. H. (2000). Intermittent mixing in strongly stratified fluids as a random walk. *Journal of Fluid Mechanics*, 411, 165–185. <https://doi.org/10.1017/S00222112099008149>
- Wang, L., & Geller, M. A. (2003). Morphology of gravity-wave energy as observed from 4 years (1998–2001) of high vertical resolution U.S. radiosonde data. *Journal of Geophysical Research*, 108(D16), 4489. <https://doi.org/10.1029/2002JD002786>
- Wang, L., Geller, M. A., & Alexander, M. J. (2005). Spatial and temporal variations of gravity wave parameters. Part I: Intrinsic frequency, wavelength, and vertical propagation direction. *Journal of the Atmospheric Sciences*, 62(1), 125–142. <https://doi.org/10.1175/JAS-3364.1>
- Wilson, R., Dalaudier, F., & Luce, H. (2011). Can one detect small-scale turbulence from standard meteorological radiosondes? *Atmospheric Measurement Techniques*, 4(5), 795–804. <https://doi.org/10.5194/amt-4-795-2011>
- Wilson, R., Hashiguchi, H., & Yabuki, M. (2018). Vertical spectra of temperature in the free troposphere at meso-and-small scales according to the flow regime: Observations and interpretation. *Atmosphere*, 9(11), 415. <https://doi.org/10.3390/atmos9110415>
- Wilson, R., Luce, H., Dalaudier, F., & Lefrère, J. (2010). Turbulence patch identification in potential density or temperature profiles. *Journal of Atmospheric and Oceanic Technology*, 27(6), 977–993. <https://doi.org/10.1175/2010JTECHA1357.1>



- Wilson, R., Luce, H., Hashiguchi, H., Nishi, N., & Yabuki, Y. (2014). Energetics of persistent turbulent layers underneath mid-level clouds estimated from concurrent radar and radiosonde data. *Journal of Atmospheric and Solar-Terrestrial Physics*, 118, 78–89. <https://doi.org/10.1016/j.jastp.2014.01.005>
- Wilson, R., Luce, H., Hashiguchi, H., Shiotani, M., & Dalaudier, F. (2013). On the effect of moisture on the detection of tropospheric turbulence from in situ measurements. *Atmospheric Measurement Techniques*, 6(3), 697–702. <https://doi.org/10.5194/amt-6-697-2013>
- WMO (World Meteorological Organization) (1957). Meteorology—A three-dimensional science. *WMO Bulletin*, 6(4).
- Wolff, J. K., & Sharman, R. D. (2008). Climatology of upper-level turbulence over the contiguous United States. *Journal of Applied Meteorology and Climatology*, 47(8), 2198–2214. <https://doi.org/10.1175/2008JAMC1799.1>
- Yoo, J.-H., Choi, T., Chun, H.-Y., Kim, Y.-H., Song, I.-S., & Song, B.-G. (2018). Inertia-gravity waves revealed in radiosonde data at Jang Bogo Station, Antarctica (74°37'S, 164°13'E). Part I: Characteristics, energy, and momentum flux. *Journal of Geophysical Research: Atmospheres*, 123, 13,305–13,331. <https://doi.org/10.1029/2018JD029164>
- Zhang, J., Chen, H., Li, Z., Fan, X., Peng, L., Yu, Y., & Cribb, M. (2010). Analysis of cloud layer structure in Shouxian, China using RS92 radiosonde aided by 95 GHz cloud radar. *Journal of Geophysical Research*, 115, D00K30. <https://doi.org/10.1029/2010JD014030>